POUSO DE MULTIRROTOR EM PLATAFORMA NÃO-INERCIAL

Ricardo Halfeld Rosadas de Andrade

Dissertação de Mestrado apresentada ao Programa de Pós-graduação em Engenharia Elétrica, COPPE, da Universidade Federal do Rio de Janeiro, como parte dos requisitos necessários à obtenção do título de Mestre em Engenharia Elétrica.

Orientador: Alessandro Jacoud Peixoto

Rio de Janeiro
Junho de 2022

POUSO DE MULTIRROTOR EM PLATAFORMA NÃO-INERCIAL

Ricardo Halfeld Rosadas de Andrade

DISSERTAÇÃO SUBMETIDA AO CORPO DOCENTE DO INSTITUTO ALBERTO LUIZ COIMBRA DE PÓS-GRADUAÇÃO E PESQUISA DE ENGENHARIA (COPPE) DA UNIVERSIDADE FEDERAL DO RIO DE JANEIRO COMO PARTE DOS REQUISITOS NECESSÁRIOS PARA A OBTENÇÃO DO GRAU DE MESTRE EM CIÊNCIAS EM ENGENHARIA ELÉTRICA.

Examinada por:

Prof. Alessandro Jacoud Peixoto, D.Sc.

Prof. Fernando Cesar Lizarralde, D.Sc.

Prof. Armando Alves Neto, D.Sc.

RIO DE JANEIRO, RJ – BRASIL
JUNHO DE 2022

Halfeld Rosadas de Andrade, Ricardo

Pouso de Multirrotor em Plataforma não-Inercial/Ricardo Halfeld Rosadas de Andrade. – Rio de Janeiro: UFRJ/COPPE, 2022.

X, 73 p.: il.; 29, 7cm.

Orientador: Alessandro Jacoud Peixoto

Dissertação (mestrado) – UFRJ/COPPE/Programa de Engenharia Elétrica, 2022.

Bibliography: p. 63 – 65.

1. Controle Suave por Modos Deslizantes. 2. Pouso Autônomo de VANT. 3. Resultados Experimentais com Drone. I. Jacoud Peixoto, Alessandro. II. Universidade Federal do Rio de Janeiro, COPPE, Programa de Engenharia Elétrica. III. Título.

Resumo da Dissertação apresentada à COPPE/UFRJ como parte dos requisitos necessários para a obtenção do grau de Mestre em Ciências (M.Sc.)

POUSO DE MULTIRROTOR EM PLATAFORMA NÃO-INERCIAL

Ricardo Halfeld Rosadas de Andrade

Junho/2022

Orientador: Alessandro Jacoud Peixoto

Programa: Engenharia Elétrica

Neste trabalho, é abordado o problema de pouso autônomo de VANTs em uma plataforma verticalmente oscilante. Um esquema robusto de controle adaptativo de altitude é proposto para lidar com o efeito aerodinâmico chamado Efeito Solo e a variação de massa durante uma tarefa de pick/place. A parte robusta do controlador é baseada no controle de modo deslizante que apresenta um sinal de controle suave, livre de *chattering*, previamente projetado para plantas lineares. Nesse sentido, este trabalho apresenta a primeira generalização deste controlador para a classe de plantas não lineares representando a dinâmica vertical do veículo. A análise de estabilidade assumindo a velocidade vertical é fornecida. O desempenho do método proposto é ilustrado por meio de simulações numéricas e resultados experimentais são obtidos com dois VANTs.

Abstract of Dissertation presented to COPPE/UFRJ as a partial fulfillment of the requirements for the degree of Master of Science (M.Sc.)

MULTIRROTOR LANDING ON NON-INERTIAL PLATFORM

Ricardo Halfeld Rosadas de Andrade

June/2022

Advisor: Alessandro Jacoud Peixoto

Department: Electrical Engineering

In this work, the problem of autonomous landing of UAVs on a vertically oscillating platform is addressed. A robust adaptive altitude control scheme is proposed to deal with the aerodynamic effect so called Ground Effect and the mass variation during a pick/place task. The robust part of the controller is based on sliding mode control that features a smooth control signal, free of *chattering*, previously designed for linear plants. In this sense, this work presents the first generalization of this controller for the class of nonlinear plants representing vertical dynamics of the vehicle. The stability analysis assuming the vertical velocity is provided. The performance of the proposed method is illustrated by means of numerical simulations and experimental results are obtained with two UAVs.

Contents

List of Figures

List of Tables

Chapter 1

Introduction

Over a decade has passed since multi-rotors, commonly referred to as "drones", have have claimed the professional and recreational markets, ranging from toys to industrial machines. They have proven to be extremely useful tools in cinematography, inspections, agriculture, public safety, logistics, among other fields. Applications have been limited to remotely-operated due airspace control, safety and mission cycle operational difficulties, which are all technical reasons, ultimately. While airspace control and safety are partially political challenges, the technical aspect can and must be worked on for when autonomous operations are finally adapted into our society.

In fact, multi-rotors have been of research interest for longer than that [1], and have continued to evolve throughout these years, with a wide range of control strategies being tested for general flight. Real-time schemes for multi-rotor control are employed in [2]. In [3], a quaternion-based control scheme for the attitude control problem is proposed, where both the multi-rotor's attitude model and a non-linear proportional squared (P2) control algorithm have been implemented without any transformations and calculations in the Euler's angle space or Direction Cosine Matrix (DCM). In [4], by explicitly taking into account the constraint of non-zero total thrust in the proposed control design, an almost global asymptotic stability of the tracking controller is guaranteed.

Off-the-shelf products have matured into reliable flight machines with miniaturized gimbaled cameras showcasing disproportional image resolution, multi-spectral capability, ultra-precise localization technology such as RTK (Real-time Kinematics) with centimeter accuracy, AI (Artificial Intelligence) for subject tracking, etc.

Less effort has been allocated into some of the supporting stages of a multi-rotor's mission. While taking-off and flying - and taking pictures and such - are optional, landing is mandatory.

To illustrate the level of difficulty in such maneuvers, even approaches for a tether-guided landing of an autonomous helicopter using an autopilot for au-

tonomous landing of a helicopter on a rocking ship, due to rough sea were considered in [5].

Autonomous landings on a moving platform using image-based visual servoing is described in [6], where a vision-based algorithm to control a multi-rotor while tracking and landing on a moving platform was developed. Vision is taking an important role in this context, as unknown movements of the landing surface, and external disturbances make it difficult to generate a relative pose estimate with sufficient accuracy for landing LING *et al.* [7]. LEE *et al.* [6] takes on the challenge of doing so without estimating the vertical distance.

Inserting the ground effect modelling, in [8] the ground effect is considered, which increases the difficulty for multi-rotors to land precisely.

Even now, one cannot count on a high-end system to consistently land itself outside of comfortably open and static environments. However remotely located an application environment is, such as agricultural and offshore fields, an operator is still required to operate multi-rotors. There is a wide space of applications just waiting for such a limitation to be lifted.

In the last few years, interest in autonomous multi-rotors has risen for logistical and environmental applications for which the combination of multi-rotors with other mobile systems is required. Autonomy in the landing maneuver is not only required for fully autonomous missions, but also as a support system in remotely-operated applications where the operator is not capable of dealing with the proximity to obstacles or the dynamic nature of the pad.

We seem to stand at the edge of a rapid expansion in the use of unmanned aerial systems working closely with society. Although envisioned at a few occasions in the last decade, they were mostly false starts as the technology only appeared to have matured tremendously, but the expansion in capacity was mainly on the core activity of the flight - usually related to visual capture - and not on making the flight cycle robust to hardships, and that is changing. On the last couple of years, a comprehensive demonstration of a robust autonomous flight cycle came to existence. While that demonstration aims at a remote application still, it boosts the imagination of what it will enable inside cities.

Conveniently, these new applications are a great fit for the robust controllers, and vice-versa. The former benefits from the research of better performing trajectory tracking controllers and the latter benefits from the dissemination of such controller syntheses [9] [10] [6] in the academy and technological markets.

Figure 1.1: M600 popping off the pad, gaining over 3m in under 2 seconds.

1.1 The landing maneuver

When taking-off, the multi-rotor starts in a state of contact with its pad. As the collective thrust increases, the contact force becomes less and less until the thrust exceeds the weight. From that point on, the acceleration is only as great as the collective thrust. The accelerations are limited and therefore designing a structure for this load case is straightforward.

Since the thrust-to-weight ratio of multi-rotor is usually plenty, popping off the pad is typically not an issue. Surely care must be taken in windy and turbulent conditions, and even more when doing so near obstacles. Rapidly leaving the pad:

- Prevents skidding and re-contacting issues leading to tipping over and unintentionally yawing.
- Minimizes disturbances such as ground-effect or pad induced turbulence.
- Increases distance to most obstacles quickly.

Landing, however, is a much greater challenge. In this maneuver, the multi-rotor transitions from a flight state to a contact state. Unlike the opposite transition, the acceleration, jerk, snap, etc. levels are determined by the approach trajectory, which must attain a minimal quality to ensure structural integrity and an upright stance until the multi-rotor is fastened to the pad. Coming in slowly can be just as bad coming in quickly.

In a perfect landing maneuver, the landing gear meets the pad at the intended touch-down (TD) time t_{TD}, at the intended position, with zero relative linear and angular velocity. All the planning must be done prior to t_{TD} and updated during the maneuver to accommodate any prediction errors or disturbances. Doing so allows the prediction of the time required to land, which translates to mission battery overhead reduction.

The maneuver starts at a holding position, where the multi-rotor is as close as possible to its touch-down position while staying clear from the pad's motions. The closer the holding position is to the touchdown position the higher the risk of

an unintended contact with the pad, although the required prediction horizon is reduced. On the other hand, keeping these two main stations further apart is safer while waiting for the right touch-down conditions, but this comes with the price of a farther prediction horizon.

The system must then log the non-inertial pad motion and begin searching for a pattern. Assuming there is a pattern to be found and also assuming the existence of a recognition technique, the ideal landing system can proceed with the required processing. At this stage, the prediction belief as a function of time is useful.

The next stage is the first planning iteration. Trajectory generation in the context of hovering machines has been thoroughly discussed in [11]. In essence, multi-rotors enjoy minimum snap trajectories. To define such a trajectory, one must simply know initial and final positions and velocities as well as bounding surfaces (typically cylinders). Extremum-seeking algorithms for real-time generation of optimal trajectories through a sequence of 3-D positions and yaw angles, while ensuring safe passage through specified corridors and satisfying constraints on velocities, accelerations and inputs are employed, followed by the use of tuned trajectory following controllers.

Another computationally efficient motion primitive for multi-rotor trajectory generation can be found in [12], while aggressive multi-rotor flight through cluttered environments using mixed integer programming is presented in [13].

In typical non-inertial landing pads, the multi-rotor would need a small touch-down stretch roughly in the vertical direction, bounded by a cylinder with the allowable landing offset radius, and another linear stretch connecting its current position to the top of the aforementioned touch-down stretch. The boundary for this stretch is defined by the distance to obstacles, which in turn determine how tall the touch-down stretch must be.

While the multi-rotor follows its planned trajectory, invisible, virtually immeasurable atmospheric features interact with its structure, disturbing the system. The impracticality of anticipating such disturbances imposes unto the controller the pursuit of robustness, all the while reminding the designer of the creeping certainty that, some day, it will not be enough. Hope for the best, but plan for the worst, as the saying goes.

Until a system which alleviates the requirement for good landings is devised, it will be imperative to introduce good abortion characteristics to the landing strategy.

1.2 Notation and Terminology

The following notation and basic concepts are employed:

(1) ISS means Input-to-State-Stable and classes $\mathcal{K}$, $\mathcal{K}_\infty$ functions are defined as

in [14].

(2) The Euclidean norm of a vector x and the corresponding induced norm of a matrix A are denoted by $|x|$ and $|A|$, respectively.

(3) The symbol "s" represents either the Laplace variable or the differential operator "d/dt", according to the context.

(4) As in [15, 16] the output y of a linear time invariant (LTI) system with transfer function $H(s)$ and input u is given by $y = H(s)u$. Convolution operations $h(t) * u(t)$, with $h(t)$ being the impulse response from $H(s)$, will be eventually written, for simplicity, as $H(s) * u$.

(5) As usual in SMC, Filippov's definition for solution of discontinuous differential equations is adopted [17].

(6) We denote by $\pi(t)$ any exponentially decreasing signal, i.e., a signal satisfying $|\pi(t)| \leq \Pi(t)$, where $\Pi(t) := Re^{-\lambda t}$, $\forall t$, for some scalars $R, \lambda > 0$.

Chapter 2

Modeling and General Control Architecture

2.1 Multi-rotor Description

During the research the following multi-rotor models were used:

- Custom built quad-rotor
- Bitcraze's Crazyflie 2.0, with Flow Deck 2.0 and Multi-ranger Deck
- DJI's Matrice 600 Pro

The first is quad-rotor with parallel motor axes. It is assembled on an F450 frame, with large propellers, uses an Atmega micro-controller for Low- and High-Level control.

The Crazyflie 2.0 is an open-source nano quadrotor designed by Bitcraze, in Sweden. Weighing only 27g, with net collective thrust up to roughly 60gf, this quadrotor is highly capable and robust. Its ability to survive crashes allows for short experimental cycles. The diversity of accessories and the well structured community of developers makes it a convenient platform for research and development in mobile robotics.

It is equipped with several sensors. Aside from the common equipment, such as IMU, radio, etc., the quadrotors used in the experiments are equipped with the Flow Deck and the LPS Deck, two modular PCBs that can be stacked with the main PCB extending its sensory capacity. The Flow Deck adds a flow sensor to measure horizontal velocity and a ranger in the vertical direction, both pointing downwards, which allows it to measure the distance to the ground. The LPS Deck uses an UWB (Ultra-Wide Band) antenna to measure the distance to anchors fixed in the environment at known locations. It serves as an absolute frame of reference for the quadrotor.

DJI's Matrice 600 Pro (M600P) is, at the time of this work, the largest aerial platform in the industrial class offered by the Chinese company. With 6 propellers, payload of 6kg, retractable landing gear, easy access to components for modifications and flight times exceeding 40 minutes, there's hardly any limitation for research and development. Its versatility is enhanced by an open C++ SDK with complete ROS wrapper.

The use of a large spectrum of multi-rotor scales provides not only a great amount of academic opportunities, but also instils generalized intuition of the dynamics of such systems.

2.2 Reference Frames

The following descriptions can become very confusing without establishing a convention. The following reference frames must be defined so that other definitions can be built upon them, see Figure 2.1.

Figure 2.1: Local ENU (East, North, Up)

- Inertial
  - Geodesic
  - Cartesian
  - ENU (East, North, Up)
- Multi-rotor
  - FLU (Front, Left, Up)
  - Body
- Sensor
  - Accelerometer
  - Gyroscope
  - GPS

Magnetometer

Barometer

Camera

- Landing Pad

  Visual Markers

Figure 2.2 presents the main reference frames attached at the drone, while Figure 2.3 illustrates the additional frames including the landing pad and the inertial reference frames.

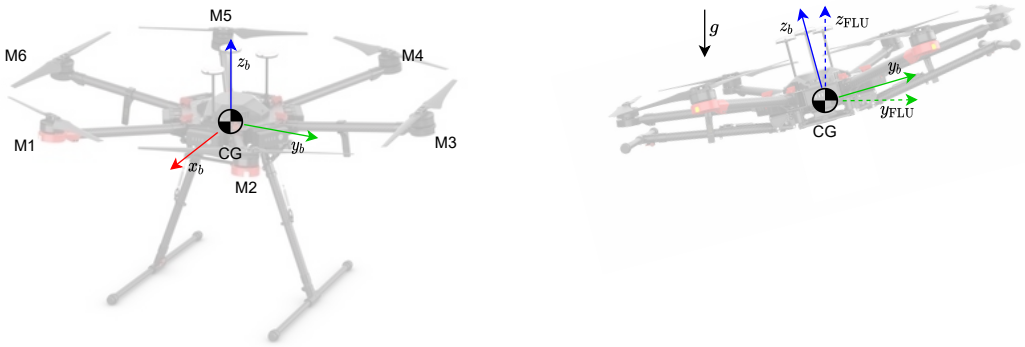

Figure 2.2: Multi-rotor Reference Frames.

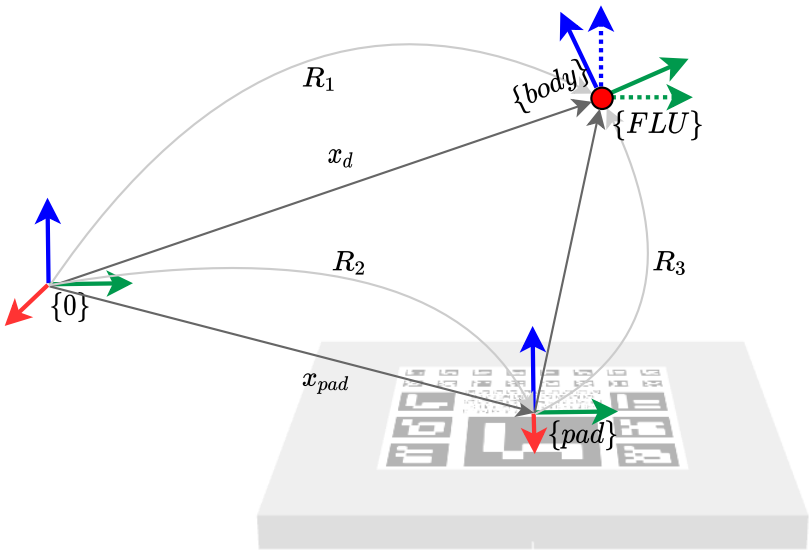

Figure 2.3: Positions and rotations between inertial, multi-rotor and pad frames.

2.3 Mathematical Model

There are several approaches to modelling this system and a few have been referenced in the bibliographic review chapter. The strategy used in this work is based on Newton-Euler method due to its inherent intuitiveness quality.

The less intuitive (at least on a first glance) use of Unit Quaternions aims to further illustrate the benefits of its use, solidify its importance in aggressive, i.e., more capable, maneuvers and hopefully clarify the properties that make the use of Unit Quaternions an ideal tool for attitude control.

The use of Unit Quaternions provides a singularity-free space, meaning there is no degradation of this representation in any possible attitude.

The following equations form the mathematical model for a multi-rotor [3]:

$$\begin{aligned} \ddot{x} &= RF_{\{b\}} + F_{\{0\}} = q^* \otimes \begin{bmatrix} 0 \\ F_{\{b\}} \end{bmatrix} \otimes q + F_{\{0\}} \,, \\ \dot{q} &= \frac{1}{2} \begin{bmatrix} 0 \\ \omega \end{bmatrix} \otimes q \,, \\ \omega &= I_{cm}^{-1} \cdot \tau - I_{cm}^{-1} \left[\omega \times (I_{cm} \cdot \omega) \right] \,, \end{aligned} \tag{2.1}$$

where x denotes the position vector of the multi-rotor mass' center, represented in the inertial frame $\{0\}$, R is the rotation matrix form the body reference frame $\{b\}$ to $\{0\}$, q is the Unit Quaternion, ω is the multi-rotor angular velocity, represented in $\{0\}$, I_{cm} is the moment of inertia, τ is the total momentum applied around the center of mass and $RF_{\{b\}} + F_{\{0\}}$ is the total force applied at the center of mass.

By inspection, one can perceive a clear distinction of translation and rotational dynamics. One may also notice a one-way causality of the rotational dynamics in the translation dynamics, i.e., there is no intrinsic influence on the vehicle's rotation by its position in the environment, however, its orientation is determinant for the translation.

To illustrate, consider a perfectly balanced multi-rotor hovering in horizontal orientation with null velocity and neglect all aerodynamic effects except for propeller thrust and torque. It remains still in this stance regardless of its initial position in space.

Now starting this very same vehicle in the same state (i.e., rotor angular velocities, landing gear position, etc.), except for a slight difference in pitch or roll, will start moving it in the direction it leans into, highlighting the effect of orientation in translation.

In the opposite causality direction, its translation does not affect its orientation in such a simplified system. The vehicle will not alter its orientation regardless

where in space it lies unless its rotors apply a moment on it.

In fact, aerodynamic effects of the vehicle's airspeed, as well as observer design do indeed influence the rotational dynamics. If the model is extended to consider surrounding air flow, then both translation and rotational dynamics become mutually coupled. These effects can be added as force and moment plugins in the mathematical model, although for most applications of multi-rotors that would be overkill.

2.4 Control Allocation

In the presented mathematical model, the inputs are the net forces and moments applied to the vehicle's body, but in reality these fold out into at least as many forces and moments as there are actuators, which can be propulsive systems, servos, aerodynamic surfaces (both active and passive), etc. In order to apply the intended net force and moment, the system needs a map between them and their actuators' states.

In the case of a pure multi-rotor (without any other relevant aerodynamic actuators and suppressing the use of actuators that are not intended for flight control, such as landing gear servos), the net force and moment can be obtained by computing the thrust T and reaction torque Q of each propeller. Therefore, one must consider a mathematical model for the propellers. A typical approach is a polynomial function (or just an exponential) of the angular velocity when the propeller is at steady state and in a fixed position.

$$\begin{aligned} T &= \frac{1}{2} C_T \omega^r \,, \\ Q &= \frac{1}{2} C_Q \omega^s \,, \end{aligned}$$

where C_T is the thrust coefficient, C_Q is the reaction coefficient and ω^s and ω^r are the propeller angular velocities at steady state and in a fixed position, with exponent s and r, respectively.

Please bear in mind that all the vectors presented in the following equations are presented in the body frame exclusively.

An individual propeller of index i with thrust coefficient C_T and exponent r pointed in the direction of the unit vector $\hat{d}_i$ at the angular velocity ω_i contributes with the thrust vector F_{Ti}, given by:

$$F_{Ti} = T_i \hat{d}_i = \left(\frac{1}{2} C_T \omega_i^r \right) \hat{d}_i \,.$$

If the i-th propeller's thrust vector is offset by a position vector l_i, it may induce

a moment component M_{Ti}, given by:

$$M_{Ti} = l_i \times T_i \hat{d}_i = l_i \times \left(\frac{1}{2} C_T \omega_i^r\right) \hat{d}_i \,.$$

Spinning the propeller's blades through the air generates a reaction torque due to their drag, which yields a moment component M_{Q_i} in the direction of d_i, with magnitude function of the coefficient C_Q and exponent s, given by:

$$M_{Q_i} = Q_i \hat{d}_i = \left(\frac{1}{2} C_Q \omega_i^s\right) \hat{d}_i \,.$$

On the other hand, while the net thrust vector is the sum of the individual thrust vectors, the net moment is the sum of the sum of reaction torque vector compounded with the sum of levered thrust vectors, such that one can write:

$$\begin{aligned} F_{net} &= \sum_{i=1}^{n} F_{Ti} \,, \\ M_{net} &= \sum_{i=1}^{n} M_{Ti} + \sum_{i=1}^{n} M_{Q_i} \,. \end{aligned}$$

Despite being the same final type, they arise from different mechanisms. Figure 2.4 illustrates all the vector's definitions.

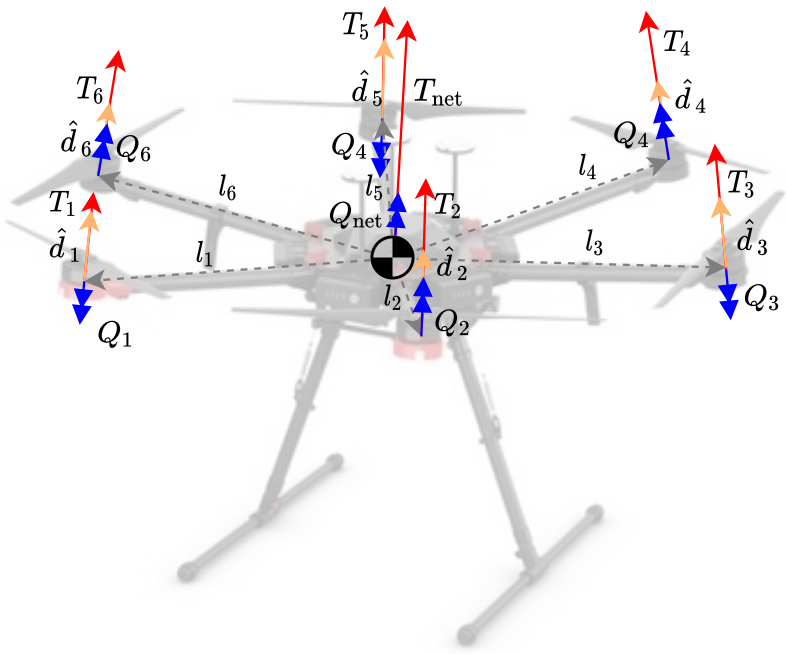

Figure 2.4: Vector Definitions.

2.4.1 Net Thrust and Net Moment

First note that, one can further write:

$$\begin{bmatrix} F_{net} \\ M_{net} \end{bmatrix} = \sum_{i=1}^{n} \begin{bmatrix} F_i \\ M_i \end{bmatrix} = \sum_{i=1}^{n} \begin{bmatrix} T_i \hat{d}_i \\ l_i \times T_i \hat{d}_i + Q_i \hat{d}_i \end{bmatrix} . \tag{2.2}$$

Since T_i and Q_i are scalars, they are free to move out of the cross product and vectors. Hence, one has that:

$$\begin{bmatrix} F_{net} \\ M_{net} \end{bmatrix} = \sum_{i=1}^{n} \left(\begin{bmatrix} T_i \hat{d}_i \\ l_i \times T_i \hat{d}_i \end{bmatrix} + \begin{bmatrix} 0 \\ Q_i \hat{d}_i \end{bmatrix} \right) = \sum_{i=1}^{n} \left(\begin{bmatrix} \hat{d}_i \\ l_i \times \hat{d}_i \end{bmatrix} T_i + \begin{bmatrix} 0 \\ \hat{d}_i \end{bmatrix} Q_i \right) . \tag{2.3}$$

With summation in matrix form and expanding T_i and Q_i, one can obtain:

$$\begin{bmatrix} F_{net} \\ M_{net} \end{bmatrix} =$$

$$\frac{1}{2} C_T \begin{bmatrix} \hat{d}_1 & \hat{d}_2 & \cdots & \hat{d}_n \\ l_1 \times \hat{d}_1 & l_2 \times \hat{d}_2 & \cdots & l_n \times \hat{d}_n \end{bmatrix} \begin{bmatrix} \omega_1^r \\ \omega_2^r \\ \vdots \\ \omega_n^r \end{bmatrix} + \frac{1}{2} C_Q \begin{bmatrix} 0 & 0 & \cdots & 0 \\ \hat{d}_1 & \hat{d}_2 & \cdots & \hat{d}_n \end{bmatrix} \begin{bmatrix} \omega_1^s \\ \omega_2^s \\ \vdots \\ \omega_n^s \end{bmatrix} \tag{2.4}$$

In addition, by allowing $r = s$, one can find a much more familiar form:

$$\begin{bmatrix} F_{net} \\ M_{net} \end{bmatrix} = \frac{1}{2} \begin{bmatrix} C_T \hat{d}_1 & \cdots & C_T \hat{d}_n \\ C_T \left(l_1 \times \hat{d}_1 \right) + C_Q \hat{d}_1 & \cdots & C_T \left(l_n \times \hat{d}_n \right) + C_Q \hat{d}_n \end{bmatrix} \begin{bmatrix} \omega_1^r \\ \omega_2^r \\ \vdots \\ \omega_n^r \end{bmatrix} . \tag{2.5}$$

While doing so simplifies the system, it can also be perceived as a constraint in the force and moment modelling of the propeller, which may introduce undesired input error in the system. In order to reach the familiar $y = Ax$ form without imposing $r = s$, one may concatenate $\begin{bmatrix} \omega_1^r & \cdots & \omega_n^r \end{bmatrix}^T$ and $\begin{bmatrix} \omega_1^s & \cdots & \omega_n^s \end{bmatrix}^T$, reaching:

$$\begin{bmatrix} F_{net} \\ M_{net} \end{bmatrix} = \frac{1}{2} \begin{bmatrix} C_T \hat{d}_1 & \cdots & C_T \hat{d}_n & 0 & \cdots & 0 \\ C_T \left(l_1 \times \hat{d}_1 \right) & \cdots & C_T \left(l_n \times \hat{d}_n \right) & C_Q \hat{d}_1 & \cdots & C_Q \hat{d}_n \end{bmatrix} \begin{bmatrix} \omega_1^r \\ \vdots \\ \omega_n^r \\ \omega_1^s \\ \vdots \\ \omega_n^s \end{bmatrix} , \tag{2.6}$$

which in turn comes at the expense of doubling the domain's dimension and turning A into a $n \times 2n$ rectangular matrix.

This algebraic problem isn't truly of dimension $2n$. It is parameterized by ω_i with $i \in \mathbb{Z} \mid (1 \leq i \leq n)$, thus constraining the effective input space to n - same as the output.

As for the range of the allocation matrix, most multi-rotors are under-actuated, rendering a non-trivial null-space. Even when the amount of actuators is greater than or equal to 6, which is the number of degrees of freedom of the vehicle's core, they are usually arranged in a way that provides redundancy, not in a way that increases the allocation matrix‘ range - that is, they all point roughly in the same direction. Therefore, even in the particular case of 6 rotors, one likely needs to synthesize a controller that nests attitude control in translation control to overcome its narrow allocation range.

It is important to note two other major sources of detachment between the propulsive model and reality: Propulsion changes with the advance through air and; the propulsive jet causes significant changes in aerodynamic forces over the surface.

The aforementioned characteristics favor a design with converging thrust direction vectors ($\hat{d_i}$). This arrangement drives both translation and rotation dynamics in harmony. Accelerating the vehicle in a given direction outside its allocation range involves leaning into that same direction, and a converging arrangement induces change in the right sense for both translation and rotation dynamics as soon as commanded. However, this may not be the most aerodynamically efficient arrangement, so this decision is strongly related to the nature of the multi-rotor‘s mission.

From a geometric perspective, it is preferable to first get the multi-rotor in an orientation that has at least some force contribution in the desired acceleration direction, and only then increase thrust. Thrust varies only to cancel out gravity throughout the attitude change. Once oriented such that the net force vector coincides in direction with the desired acceleration vector, full thrust should be applied. This ensures minimal radial deviation.

Whether to start applying thrust from the moment the net thrust vector‘s projection into the desired acceleration vector is positive or only when it is pointing exactly parallel to it is determined by the spatial constraints of the maneuver. It serves no purpose to wait until the attitude is just right to apply full thrust when this means the multi-rotor will collide with a plane normal to the desired acceleration vector, nor does applying full thrust just as it passes the quadrature orientation if the induced deviation in that direction will cause it to collide with a cylindrical object also defined by that direction.

2.5 Measurements and Estimations

The content of this section aims to provide insight and illustrate a possible observer design. It does not necessarily describe the observer implementation of the aforementioned multi-rotors, which likely changes case to case.

Despite the explosive advances in inertial measurement technology boosted by cellphone R&D, sensors by themselves are still not enough for attitude determination, let alone positional. However, the lower cost per measurement device allows designers to group complementary sensors onboard, which condition the application of estimation filters.

As discussed in the mathematical modelling section, position, orientation and their derivatives are the system's main states. Measurements are challenging, each in its own way. Positional measurements suffer from low update rates as well as a large amount of sources of error, velocities lack useful and self contained devices, angular velocities are haunted by bias and direct orientation devices are cross-disturbed with other states. Together, however, they provide a trustworthy estimation platform.

A simple example of such complementary action is an attitude estimator conveniently referred to as Complementary Filter. In its implementation, a gyroscopic measurement device is used in conjunction with an accelerometer. The former measures angular velocity with virtually no delay, but suffers from electrically and thermally induced bias. The latter gives an inaccurate and noisy measurement of the vertical direction. Designing an estimator based on both works surprisingly well for attitude measurement in small acceleration systems, such as cellphones.

Depending on the expected usage, this may very well be enough for a multi-rotor, although limiting to small accelerations is clearly leaving too much on the table. The main issue with a Complementary Filter for attitude estimation of multi-rotors is the interference of the linear acceleration in the vertical update. Bad attitude estimation during aggressive maneuvers is a bad setup.

To solve this, one needs to employ a better system model (such as the non-linear quaternion model) and ideally more and/or better update sources, such as RTK (Real-Time Kinematics), horizon identification, visual markers, etc.

2.6 General Control Architecture

In this section, the general control schemes considered in this work are briefly introduced to provide a wide idea of the control architecture (see Figure 2.6) for the mission control illustrated in Figure 2.5.

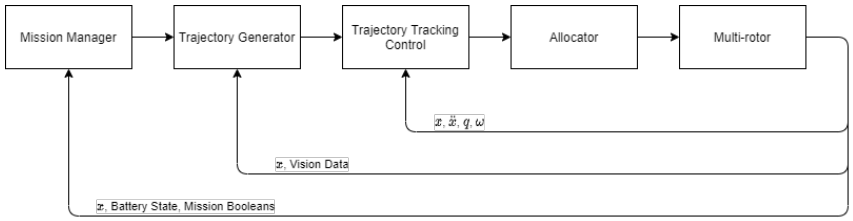

Figure 2.5: Mission Control Overview.

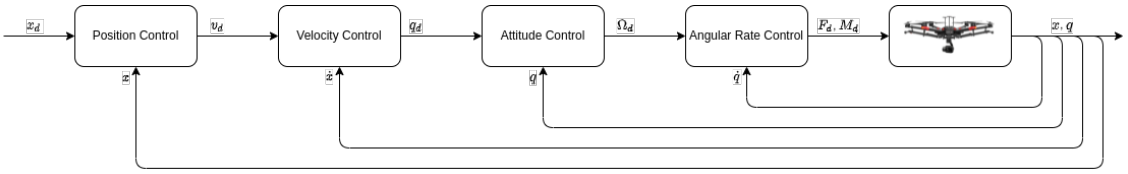

Figure 2.6: Multi-rotor Controller Diagram.

2.6.1 Attitude Control Architecture

At the heart of the control system is the attitude controller. All relevant states of the multi-rotor can be controlled by changing its orientation and net thrust in coordinated fashion, thus having a robust and well-tuned attitude controller is paramount to its performance. The desired attitude q_d is referenced by the same frame as q, i.e., q_d represents the desired orientation of the body frame with respect to the inertial frame.

Quaternions can be Kronecker multiplied to compound sequential rotations. If the unit quaternions p and q represent two possible rotations of a body with respect to the same given frame, the resulting quaternion q_{res} represents a single rotation in that same frame that will bring the body to the orientation after first applying the rotation of q, then applying the rotation of p, and can be expressed as:

$$q_{res} = p \otimes q \,. \tag{2.7}$$

Notice quaternion multiplication is non-commutative, just like rotations are non-commutative.

For completeness, the Kronecker Product can be computed in the following form using Skew Symmetric Matrices:

$$p \otimes q = \begin{bmatrix} p_0 & -p_1 & -p_2 & -p_3 \\ p_1 & p_0 & -p_3 & p_2 \\ p_2 & p_3 & p_0 & -p_1 \\ p_3 & -p_2 & p_1 & p_0 \end{bmatrix} \begin{bmatrix} q_0 \\ q_1 \\ q_2 \\ q_3 \end{bmatrix} = \begin{bmatrix} q_0 & -q_1 & -q_2 & -q_3 \\ q_1 & q_0 & q_3 & -q_2 \\ q_2 & -q_3 & q_0 & q_1 \\ q_3 & q_2 & -q_1 & q_0 \end{bmatrix} \begin{bmatrix} p_0 \\ p_1 \\ p_2 \\ p_3 \end{bmatrix} . \tag{2.8}$$

Now consider the resulting quaternion q_{res} represents the desired orientation and

q represents the current orientation. This means p represents a single rotation that would bring the body from its current orientation to the desired orientation.

The difference between the desired attitude q_d and the current attitude q can be expressed as:

$$q_e = q \otimes q_d^* \,, \tag{2.9}$$

where q_d^* is the conjugate quaternion and the vector part of q_e gives the driving direction for the controller, acting as a proportional controller.

One must simply represent it in the body frame. However, proportional action alone does not address the second order effects of a rotating body. Energy dissipation is required, otherwise the body might oscillate indefinitely.

In translation dynamics, such behavior is driven by the derivative of the position. Likewise, one may apply a moment proportional to the angular velocity, but opposite in direction, to dampen the rotation. The angular velocity is typically measured in the body frame and is also an observer state in multi-rotors.

2.6.2 Acceleration Control Architecture

The relationship between multi-rotor acceleration a, gravity g and net thrust F_{net} obeys:

$$a = \frac{F_{net}}{m} + g \,. \tag{2.10}$$

Figure 2.7 illustrates the acceleration vectors and velocity vectors along a general flight. Therefore, the required net force vector F_{netreq} in the inertial frame can be computed as:

$$F_{netreq} = m \left(a_{des} - g \right) \,, \tag{2.11}$$

where a_{des} is the desired acceleration profile.

Since acceleration is measured on-board, the error between actual acceleration a and the internal estimate $\hat{a}$ (or $\bar{a}$ if signal-to-noise ratio is good enough) can be used to adjust the required net force within reason. By introducing the acceleration feedback, the controller is able to handle small mass errors as well as aerodynamic day-to-day differences, see Figure 2.8.

2.6.3 Velocity Control Architecture

Arguably the most useful control method for a multi-rotor is velocity control. It only makes sense that this is the default remote control interface for most, if not all, multi-rotors in the market. Lower control levels, such as attitude control or even angular rate control, have too fast dynamics for most people, but from velocity and up, the dynamics are far more palatable.

Figure 2.7: DJI M600 Pro Accelerating in level flight. In (a) and (b): Red arrow represents gravity, green arrow represents net aerodynamic acceleration, blue arrow represents net acceleration. In (c)–(e): Purple arrows represent velocity vectors at each instant.

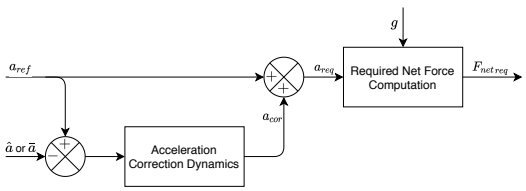

Figure 2.8: Acceleration Control Scheme.

Even though radial velocity can be measured through Doppler effect and tangential through optical flow , such sensors are rarely found in aerial robotics. Usually velocity is estimated though the use of some implementation of a Kalman Filter fed with inertial and positional measurements, e.g., GPS.

2.6.4 Horizontal Position Control Architecture

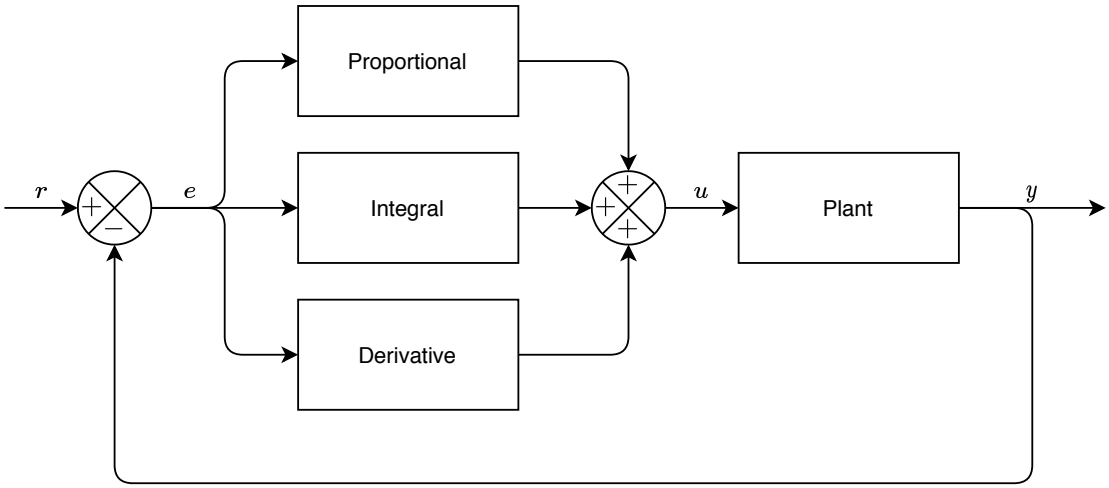

Figure 2.9: Proportional, Integral and Derivative (PID) general block diagram.

In case of multi-dimensional control, it is important to apply any saturation to the error vector, i.e., the direction must be preserved while the magnitude can be clipped. The general PID structure (with anti-windup) is applied for the horizontal position regulation control, see Figure 2.9.

2.6.5 Vertical Position Control Architecture

For the vertical position the Smooth Sliding Control (SSC), detailed in Section 4, has been implemented. The SSC is a model reference sliding mode controller, see Figure 2.10 for a general idea of the closed loop system.

Please notice that the variables $y(t)$ and $Y(s)$ do not necessarily refer to the position component y defined in the reference frames. In the theoretical scope of the SSC characterization, they represent the output signal of a plant and its Laplace transform, i.e., $Y(s) = \mathcal{L}\{y(t)\}$, with $Y(s) = H(s)U(s)$.

As traditionally defined in Model Reference Adaptive Control (MRAC), the tracking error is given by:

$$e(t) = y(t) - y_r(t)\,, \tag{2.12}$$

where y_r is the desired output signal to be tracked. When the relative degree is unitary, *sigma* is the so-called *ideal sliding variable*. In case of higher relative

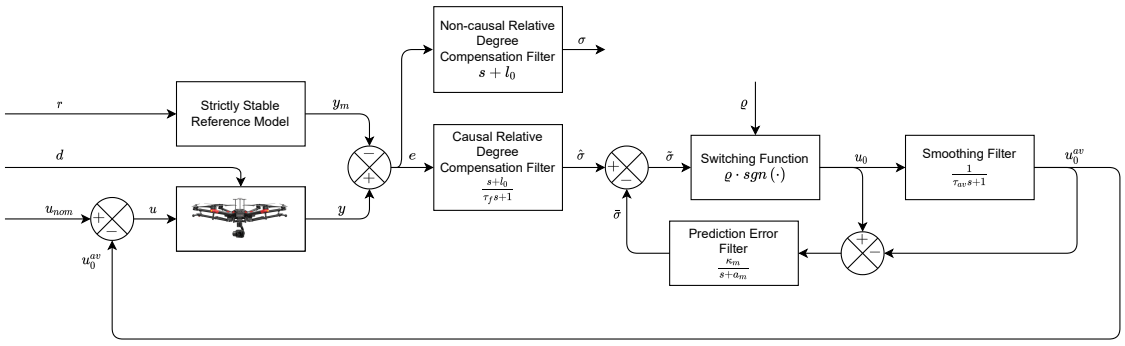

Figure 2.10: General Smooth Sliding Control (SSC) block diagram.

degree, a compensation filter is required. A non-causal filter would be the ideal choice, however one cannot implement a real-time non-causal filter. Instead, poles are added such that the frequency response is similar to the ideal non-causal filter. In the case of relative degree 2, the following filter is sufficient:

$$L(s) = \frac{s + l_0}{\tau_f s + 1} \approx s + l_0 \,. \tag{2.13}$$

2.6.6 Trajectory Tracking Control Architecture

Trajectory tracking is, in essence, defining the error dynamics in such way that the tracking error is driven to zero and stays null. As a second order control design example, the idea is to design α and β such that the following e-dynamics be stable:

$$\ddot{e}(t) + \alpha \dot{e}(t) + \beta e(t) = 0 \,, \tag{2.14}$$

where the tracking error is defined here, for example, as the difference between a reference r and an general output x, as:

$$e(t) = r(t) - x(t) \,. \tag{2.15}$$

In this case, the time-derivative of the error is expressed as

$$\dot{e}(t) = \dot{r}(t) - \dot{x}(t) \,, \tag{2.16}$$

while, the second time-derivative, satisfies

$$\ddot{e}(t) = \ddot{r}(t) - \ddot{x}(t) \,. \tag{2.17}$$

Given that the M600 Pro can be fed a desired velocity signal and shows significantly faster attitude dynamics than translation dynamics, assume the dynamics to reach

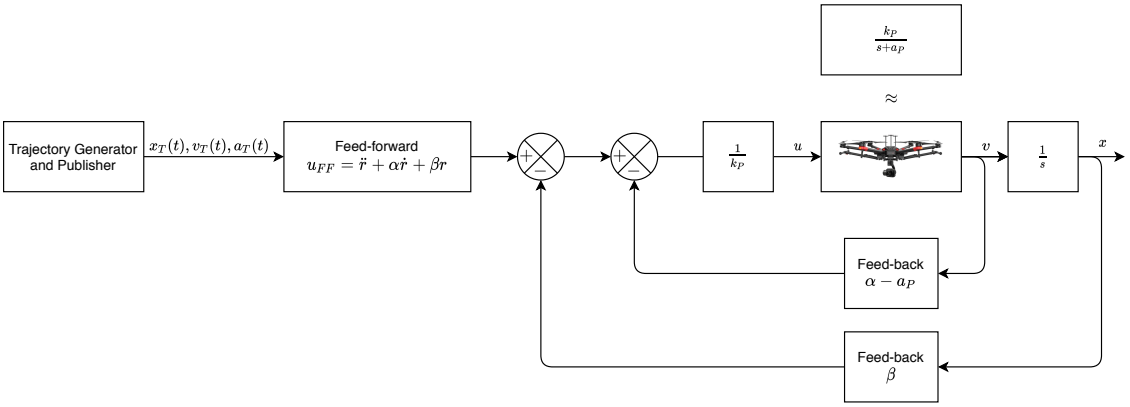

Figure 2.11: Trajectory Tracking Control for Velocity Input on M600 Pro.

the desired velocity is a 1st-order system with transfer function:

$$P(s) = \frac{k_P}{s + a_P}\,, \tag{2.18}$$

such that

$$V(s) = P(s)U(s) = \frac{k_P}{s + a_P}U(s)\,. \tag{2.19}$$

Recalling that $v = \dot{x}$, one can write that

$$X(s) = \frac{1}{s}P(s)U(s) = \frac{k_P}{s^2 + a_P s}U(s)\,, \tag{2.20}$$

or, equivalently, by multiplying by the right-side denominator $(s^2 + a_P s)$:

$$\left(s^2 + a_P s\right)X(s) = s^2X(s) + a_P sX(s) = k_P U(s)\,. \tag{2.21}$$

In time-domain, the following relationships hold:

$$\ddot{x}(t) + a_P\dot{x}(t) = k_P u(t)\,, \tag{2.22}$$

and

$$\ddot{x}(t) = -a_P\dot{x}(t) + k_P u(t)\,. \tag{2.23}$$

Moreover, from (2.15)–(2.17) and (2.14), one can obtain the control law which assures the desired e-dynamics:

$$u(t) = k_P^{-1}(\dddot{r}(t) + \alpha\ddot{r}(t) + \beta\dot{r}(t) - (\alpha - a_P)\,\ddot{x}(t) - \beta\dot{x}(t))\,. \tag{2.24}$$

From this point on, it is a matter of identifying a useful transfer function for the desired velocities to actual velocities dynamics. These can be obtained through experimental maneuvers such as step input, periodic input (sines, saw-tooth, etc.)

or any other meaningful motion.

Once these transfer functions are identified, the coefficients α and β can be arbitrarily chosen to suit the needs of the mission, which fully defines the control law in (2.24).

The additional cost of having a trajectory tracking controller is needing to plan the trajectory in such a way that provides accurate derivatives then having to sample not only the reference, but the derivatives themselves.

2.6.7 Velocity Control Field Shaping Architecture

At the core of the challenge of landing a multi-rotor on a non-inertial pad is dealing with external perturbations. Perfect knowledge of the system could allow for some precise maneuvers in absolutely controlled environments, but it is unpractical, as of now, to have accurate information of the incoming turbulence. This must be considered in order to push the envelope of such a system.

As an exercise to test how such considerations come to practice, a method for landing the multi-rotor has been synthesized based on strictly feedback control. The idea is to plan a descent and ascent pattern as a function of how well the vehicle manages to keep its horizontal position. If the vehicle is within a reasonable region, it descents. If by any means it drifts outside this region, it ascends.

This also helps to keep the visual markers in sight. By going up, the pad remains within the field of view. If the multi-rotor is well centered, approaching the pad does not cause a loss of visual localization.

The ascent/descent rate is modulated by the horizontal position, as well as other factors that will be introduced later. The inherent transport delay in the vehicle's control system filters out high frequencies in the input, which is a beneficial effect.

Consider a well-tuned horizontal position control system. In this context, a PID performs reasonably well, damping motion while regulating and even adjusting for low-frequency wind variation. The proportional part pulls the multi-rotor towards its intended horizontal position, the integral term compensates for the bias caused by the wind and the derivative action dampens the motion. With such a horizontal controller in place, the following control law for vertical velocity can be implemented the following combination of multiple behaviors (terms):

$$v_{z_d} = v_{rational} + v_{conical} + v_{aversive}\,, \tag{2.25}$$

where the terms $v_{rational}$, $v_{conical}$ and $v_{aversive}$ are explained in what follows.

The **first term** is a rational function, see Figure 2.12. As such, its output is very close to zero for the most part, with a spike at zero input. These are useful features for a quick descent (thus the negative sign) when the vehicle is regulating

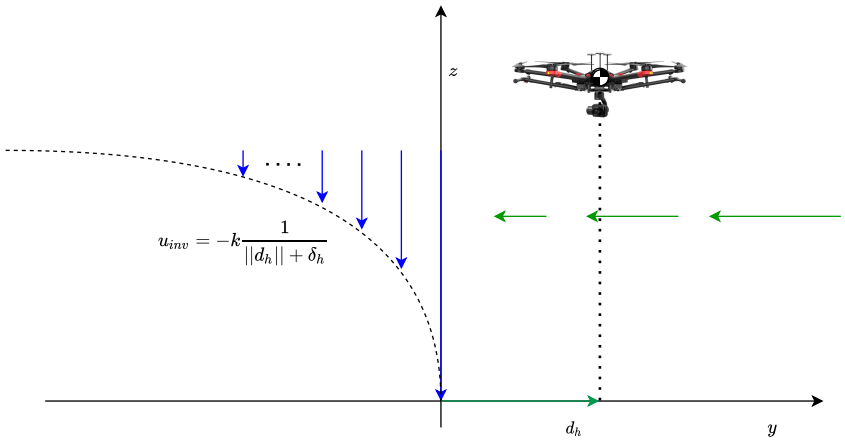

Figure 2.12: Rational (Quotient) vertical control effort term.

its horizontal position well. It allows the control to transition smoothly from not descending at all when the horizontal regulation is poor to descending as fast as allowed when exactly above the target. The following control law assures this kind of behaviour:

$$v_{rational} = -k_r \frac{1}{\|d_h\| + \delta_h}\,, \tag{2.26}$$

where $\|d_h\|$ is the horizontal distance between a reference point in the vehicle (center of mass, for instance) and the center of the landing pad, $\delta_h > 0$ is a design small positive constant used to avoid division by zero and $k_r > 0$ is a control design gain. Since pitch and rolling the frame of reference would introduce a disturbance in this measurement, it is important to calculate it in a horizontal frame. The ideal frame of reference is the FLU frame. Its Z axis is vertical and its X axis points forward. Consequently the Y axis points left, as per right hand convention.

In order to keep a compact set of frames, this FLU frame is attached to the aircraft. Other similar reference frames may be proposed, such as a FLU frame attached to the landing pad. The former is adequate for a moving target approach, whereas the latter is adequate for pad related applications. Either way, the observer performance is key to having a clean input. Luckily, multi-rotors are one of the best contexts for attitude observers.

The **second term** is a vertically offset conical surface, see Figure 2.13. The offset provides a negative region. This is a convenient way to introduce some positive vertical control if the aircraft drifts away from the center of the pad while low. Staying low increases the odds of colliding against an obstacle or tripping in the landing pad itself. Climbing, up to a certain height, also helps to keep the landing pad within the cameras' field of view. This part determines how wide the approach corridor is, so it is also possible to correlate to the vertical distance to pad in order to narrow this corridor down as needed while keeping it comfortably wide further

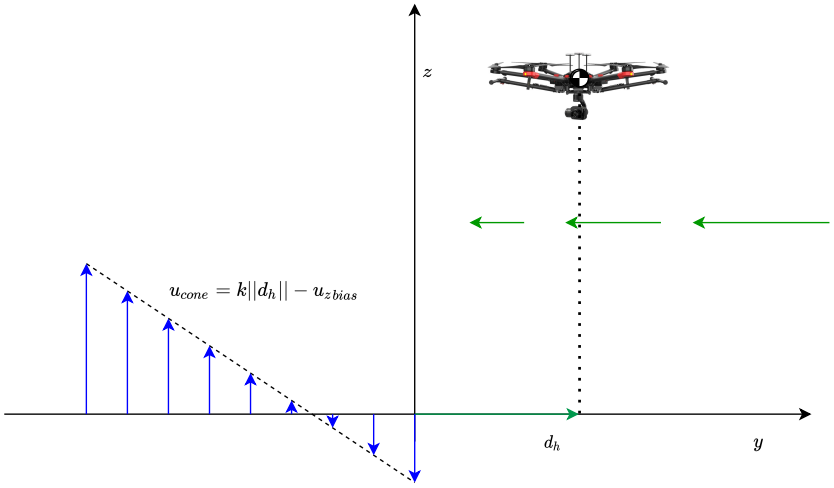

Figure 2.13: Conical vertical control effort term.

away. The following expression is proposed:

$$v_{conical} = k_c \|d_h\| - u_{zbias}\,, \tag{2.27}$$

where $k_c > 0$ is a control design gain.

The aforementioned terms would be enough for a horizontal pad with heaving motion only. The case of a pad with rolling and pitch motions as well, however, can benefit from an **extra term** to induce and **aversive action** against extreme angular motion. An asymmetric touch-down forces the multi-rotor to tumble towards the low side and seems to be the easiest way to tip over during a landing.

The following expression is proposed for the **aversive term**:

$$v_{aversive} = \frac{k_a}{\|z\| + \delta_a} \|(d_h)_{PAD}\|\,, \tag{2.28}$$

where $k_a > 0$ is a control design gain, $\delta_a > 0$ is a design small positive constant used to avoid division by zero and $(d_h)_{PAD}$ is the vector representing the distance from the pad to the drone, represented at the landing pad reference frame.

Chapter 3

Problem Formulation: Thrust Command

For the position and attitude control of a UAV a hierarchic nested control loop scheme is employed. The inner loop controls attitude while the outer loop controls position, regulating the UAV over the landing pad. State feedback control with feedforward action is employed for this goal.

This work emphasis relies on the altitude control for landing. The landing pad is assumed to be planar and sufficiently larger than the UAV. The landing problem will be interpreted as tracking problem regarding the desired trajectory z_d. For simplicity, without affecting the essence of the problem, the landing pad motion is described as a pure sine:

$$z_d(t) \;=\; \frac{A}{2}\sin(\omega t) + \frac{A}{2}\,, \tag{3.1}$$

with z_d as pad height in the inertial reference frame ($\{A\}$), A the oscillation amplitude $[m]$ and ω the oscillation frequency $[rad/s]$.

Symmetrical Ground Effect

The Ground Effect will be the same in all actuators (Symmetrical Ground Effect), depending solely on the center of gravity (C.G.) altitude w.r.t. to the landing pad. Such effect will be modelled by a same gain $k_g(z,t)$ applied to the thrust produced by each actuator, where the second argument in t is due to the landing pad vertical position $z_d(t)$ which is considered as an exogenous function of time.

To address the presence of the Symmetrical Ground Effect, consider the following hypothesis:

(H1.a) The gain $k_g(z,t)$ due to Ground Effect on each actuator are equal and depend only on the C.G.'s altitude z and landing pad vertical position $z_d(t)$.

(H1.b) The gain $k_g(z,t)$ is a smooth and continuous function in t and is such that $|k_g(z,t)| \to \infty$ as $z \to z_d$.

(H1.c) The gain k_g is unknown, subject to $k_{g_{min}} \leqslant k_g(z(t),t) \leqslant k_{g_{max}}, \forall t > 0$, being $k_{g_{min}}, k_{g_{max}}$ known positive constants.

The Ground Effect gain applied to the generated thrust of each actuator is a function of its relative height to the ground and its dimensions. For small scale UAVs (compared to the landing pad) and planar landing pads, the relative actuator altitude can be considered equal for small attitude changes, i.e., small roll and pitch angles. Therefore, under the assumption of small roll and pitch angles for attitude control during the landing, **(H1.a)** does not over constrain the problem.

For the simulations presented here, the following model for k_g is assumed [18]:

$$k_g(z,t) = \frac{1}{1 - \rho\left(\frac{R}{4(z - z_d(t))}\right)^2}, \tag{3.2}$$

with R as propeller radius and ρ as a constant characterized by geometric dimensions. Note that, with this choice for k_g, **(H1.b)** holds and **(H1.c)** is reasonable since $k_{g_{min}} \approx 1$ when the UAV is sufficiently far from the pad ($|z - z_d| \gg 2R$), and $k_{g_{max}}$ is enforced by the landing gear, and can be obtained by a static experiment.

Pick-and-Place of Payload

The UAV's total mass changes during pick-up and release operations of a payload. With such operations under regard, consider the following additional hypothesis:

(H2.a) The UAV's C.G. velocity in the inertial frame of reference is small throughout the pick-up/release operation and the mass transfer represents a smooth variation, i.e., $\dot{m}(t)$ is a smooth function norm bounded by a sufficiently small positive constant $\Delta_{\dot{m}_{max}}$.

(H2.b) The mass variation is unknown, norm bounded by a positive constant $\Delta_{m_{max}}$, and punctual in such way that the UAVs inertia moment is unaffected.

Hypothesis (**H2.a**) ensures the mass time variation can be disregarded by the translational dynamics. This is a reasonable assumption as the landing trajectory can be set to be slow and the position controller can be tuned to regulate it on the desired landing point. It is valid even when disturbances are present because a robust control scheme can be employed for position. Prior knowledge of the payload to be picked-up/released, suitable landing gear and small movements allow (**H2.b**) to be satisfied, clearly.

3.1 Dynamics of the UAV

From the well-known Newton-Euler method, both translational and rotational dynamics including the Ground Effect are obtained as :

$$\begin{aligned}
\ddot{\phi} &= \dot{\theta}\dot{\psi}\left(\frac{I_y - I_z}{I_x}\right) + k_g\frac{M_x}{I_x}\,, \\
\ddot{\theta} &= \dot{\phi}\dot{\psi}\left(\frac{I_z - I_x}{I_y}\right) + k_g\frac{M_y}{I_y}\,, \\
\ddot{\psi} &= \dot{\theta}\dot{\phi}\left(\frac{I_x - I_y}{I_z}\right) + k_g\frac{M_z}{I_z}\,, \\
m(t)\ddot{x} &= (\cos\psi\sin\theta + \cos\theta\sin\phi\sin\psi)k_g F_z\,, \\
m(t)\ddot{y} &= (\sin\psi\sin\theta - \cos\psi\cos\theta\sin\phi)k_g F_z\,, \\
m(t)\ddot{z} &= -m(t)g + (\cos\psi\cos\theta)k_g F_z\,,
\end{aligned} \tag{3.3}$$

where I_x, I_y and I_z are the moments of inertia of the UAV, M_z, M_y and M_z are the control torques for attitude dynamics, g is the acceleration due to gravity, ϕ, θ and ψ are the Euler angles (roll, pitch and yaw), x, y and z are the multi-rotor position, m is the total UAV mass and F_z is the z component of the resulting thrust $F_z^b = \begin{bmatrix} 0 & 0 & F_z \end{bmatrix}^T$ in the Body reference frame ($\{B\}$). The terms $\dot{m}(t)\dot{x}$, $\dot{m}(t)\dot{y}$ and $\dot{m}(t)\dot{z}$ were disregarded due to (**H2.a**), since $\dot{x}, \dot{y}$ and $\dot{z}$ can be considered small as well as $\dot{m}(t)$.

3.2 Altitude Dynamics

The altitude dynamics can be expressed as [19]:

$$\ddot{z} = \frac{1}{\Theta^*(t)}u(t) + d(t)\,, \quad \Theta^*(t) := \frac{m(t)}{k_h(t)k_g(z(t),t)}\,, \tag{3.4}$$

with $k_h(t) := \cos(\phi(t))\cos(\theta(t))$, control variable $u(t) := F_z(t)$ and $d(t) = -g$ interpreted as an input disturbance. Notice that $\phi(t)$ and $\theta(t)$ are exogenous signals. Under the assumption of small roll and pitch angles due to the attitude controller during landing, we obtain $\Theta^*(t) > 0$, $\forall t$. Clearly, if $\phi(t)$ and $\theta(t)$ are measured signals the effect of $k_h(t)$ in the z dynamics (3.4) can be compensated.

It must be highlighted that the input disturbance $d(t)$ could incorporate the term $\dot{m}(t)\dot{z}$ without affecting the following analysis and design. However, for simplicity and since it is reasonable to assume that $\Delta_{\dot{m}_{max}}$ in **(H2.a)** is small as well as $\dot{z}$, as mentioned before, only the acceleration g was incorporated in the input disturbance d.

3.3 Control Objective

We consider that state feedback controllers are previously employed for position (x, y) and attitude regulation, so that the focus is the vertical movement and the goal is to design a control law u that ensures asymptotic convergence of the output error (or tracking error) to zero or close to zero, defined as

$$e(t) := z(t) - z_r(t)\,, \tag{3.5}$$

keeping all closed-loop system signals uniformly bounded, regardless of uncertainties. The reference trajectory for the vehicle is given by:

$$z_r(t) := z_d(t) + z_{r_{bias}} + z_{r_{init}} e^{-t/\tau_{z_r}}\,, \tag{3.6}$$

with $z_{r_{init}} > 4R$ the initial approach altitude such that the Ground Effect is negligible, $\tau_{z_r} > 0$ is a constant such that the approach to the ground is considerable smooth. From a practical standpoint, $z_{r_{bias}}$ is a compensation for the landing gear height.

Chapter 4

Smooth Sliding Control

The Smooth Sliding Control scheme was proposed in [9] as a solution to avoid chattering, by designing a smooth control effort, in the Variable Structure Model Reference Control (VS-MRAC), a VSC strategy based on the framework of the conventional Model Reference Adaptive Control (MRAC).

The challenge of this technique is to overcome the implementation difficulties regarding VSC.

Variable structure controllers have a well-known undesirable phenomenon named *chattering* induced by non-idealities like small delays or unmodeled plant dynamics.

The *SSC* is a version of the Variable Structure Model Reference Control (VS-MRAC) based on the framework of the conventional Model Reference Adaptive Control (MRAC).

The *SSC* in [20] was generalized for linear plants with arbitrary relative degree in [21] [22]. However, to the best our knowledge, this is the first work which considers the applicability of the SSC to the class of non-linear plants considered here.

The controller topology is presented in Figure 4.1, where the output error associated with a prediction error loop ($\bar{\sigma}$), plays an essential role in avoiding chattering since it allows an ideal sliding mode (ISM) to be realized, even in the presence of the smooth filter used to filter out the switching component since the sliding mode loop is established in the inner prediction error loop ($\tilde{\sigma} \equiv 0$).

If the relative degree of the sliding variable ($\tilde{\sigma}$) is unitary[1], a ideal sliding loop is formed around the switching function and, consequently, the sliding variable tends exponentially or in finite time to zero.

Moreover, the SSC can be tuned to avoid high-gain loops and therefore can lead to chattering in the presence of unmodelled dynamics [23], in contrast with the high gain control schemes in which chattering may arise immediately for any small delay added by the unmodelled dynamics.

[1]It means that the relative degree is one around the relay, i.e., from the sliding variable (relay input) to the relay output.

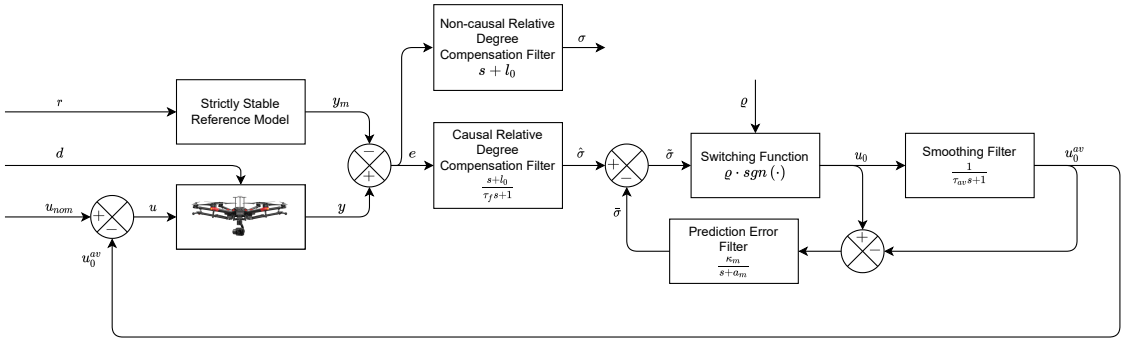

Figure 4.1: Smooth Sliding Control block diagram. The predictor block is given in (4.5), while smooth filter in (4.7). The relative degree one variable σ is defined in (4.2) or by the non-causal operator $L(s) = s + l_0$.

Despite that the SSC can be applied for a broader class of plants with arbitrary relative degree [24] and [25], omitted here for sake of clarity, we focus on the relative degree one and relative degree two cases.

Recalling the output tracking error defined in (3.5):

$$e(t) := z(t) - z_r(t)\,, \tag{4.1}$$

where z_r is the reference signal, which is a uniformly bounded signal by construction.

Let n^* be the relative degree from the SSC signal u (F_z) to the output tracking error e. When $n^* = 1$, the output tracking error can be directly used to define the sliding variable. However, when $n^* > 1$, we consider a linear (non-causal) operator $L(s) = s^{n^*-1} + l_1 s^{n^*-2} + \ldots + l_{n^*-1}$ (Hurwitz polynomial), such that the *ideal output variable* defined as:

$$\sigma(t) := L(s)e(t)\,, \tag{4.2}$$

has relative degree one from u_s. However, it is clear that the signal σ is not measured and cannot be directly applied to design the sliding variable. One possible approximation is given by

$$\hat{\sigma}(t) = L_f(s)e(t) := \frac{L(s)}{F(\tau_f s)}e(t)\,, \tag{4.3}$$

where the approximation filter $F^{-1}(\tau_f s)$ is a low pass filter with $F(\tau_f s)$ being a

Hurwitz polynomial in $\tau_f s$ with order $n^* - 1$ and unit DC gain given by $F(\tau_f s) := (\tau_f s + 1)^{n^*-1}$.

Therefore the sliding variable $\tilde{\sigma}$ is defined as,

$$\tilde{\sigma} := \hat{\sigma} - \bar{\sigma}\,, \tag{4.4}$$

where $\bar{\sigma}$ is the output of the prediction error loop and satisfies:

$$\dot{\bar{\sigma}} = -a_m \bar{\sigma} + \kappa_m (u_0 - u_0^{av})\,, \tag{4.5}$$

with $a_m, \kappa_m > 0$ being design constants.

The control law is given by:

$$\begin{aligned} u &= u_{nom} - u_0^{av}\,, & (4.6)\\ \tau_{av}\dot{u}_0^{av} &= -u_0^{av} + u_0\,, & (4.7)\\ u_0 &= \varrho(t)\mathrm{sgn}(\tilde{\sigma})\,, & (4.8) \end{aligned}$$

where u_{nom} is the nominal control law, initially designed with the knowledge of the nominal parameters of the plant, ϱ is the modulation function, $\tilde{\sigma}$ is the sliding variable and u_0^{av} is the filtered signal of the switching control u_0.

It is worth to mention that, for a sufficient small time constant τ_{av}, u_0^{av} is an approximation of the extended equivalent control $(u_0)_{eq}$, when an ideal sliding mode occurs [26].

The only restriction imposed for u_{nom} is given by the following assumption:

(H3) A set of constants $c_{nom1}, c_{nom2}, c_{nom3} \geq 0$ exists such that:

$$\|u_{nom}\| \leq c_{nom1}\|\sigma\| + c_{nom2}\|\tilde{\sigma}\| + c_{nom3}\,,$$

modulo vanishing terms.

Assumption **(H3)** is not restrictive in the sense that it allows uniformly bounded nominal controllers and dynamic nominal controllers ISS w.r.t. σ and $\tilde{\sigma}$.

The following lemmas can be stated.

Lemma 1 (ISpS property from u_0^{av} to $\bar{\sigma}$) *Consider the $\bar{\sigma}$-dynamics (4.5) with averaging control u_0^{av} in (4.7). Then, (4.5) is ISpS with respect to u_0^{av} and gain equal to $2\kappa_m\tau_{av}$. Moreover, the following inequality holds*

$$|\bar{\sigma}| \leq \omega_a + \kappa_m\tau_{av}|u_0^{av}|, \tag{4.9}$$

where

$$\dot{\omega}_a = -a_m\omega_a + a_m\kappa_m\tau_{av}|u_0^{av}|\,,$$

with $\omega_a(0) = |\bar{\sigma}(0) - \kappa_m\tau_{av}u_0^{av}(0)|$.

Proof: See Appendix A. From (4.7), one has that $u_0 - u_0^{av} = \tau_{av}\dot{u}_0^{av}$, then the prediction error dynamics can be rewritten as $\dot{\bar{\sigma}} = -a_m\bar{\sigma} + \kappa_m\tau_{av}\dot{u}_0^{av}$. By defining the auxiliary signal $\sigma_a := -\kappa_m\tau_{av}u_0^{av} + \bar{\sigma}$, one also has that $\dot{\sigma}_a = -a_m\sigma_a + a_m\kappa_m\tau_{av}u_0^{av}$. Then, by applying Lemma 11 to the σ_a-dynamics, one has that $|\sigma_a| \leq \omega_a$, where

$$\dot{\omega}_a = -a_m\omega_a + a_m\kappa_m\tau_{av}|u_0^{av}|\,, \quad \omega_a(0) = |\sigma_a(0)|\,.$$

Moreover, recalling that $\bar{\sigma} = \sigma_a + \kappa_m\tau_{av}u_0^{av}$, one has that $|\bar{\sigma}| \leq |\sigma_a| + \kappa_m\tau_{av}|u_0^{av}|$ and the following upper bound holds

$$|\bar{\sigma}| \leq \omega_a + \kappa_m\tau_{av}|u_0^{av}|\,.$$

Since, the ω_a-dynamics is linear with $a_m > 0$, it is ISS w.r.t. u_{av} with an ISS gain $\kappa_m\tau_{av}$ and the following inequality holds

$$|\omega_a(t)| \leq \pi_{\omega_a} + \kappa_m\tau_{av}\|u_0^{av}\|\,, \tag{4.10}$$

where $\pi_{\omega_a} := |\sigma_a(0)|e^{-a_m t}$ is an exponentially vanishing function and $\sigma_a(0) = \bar{\sigma}(0) - \kappa_m\tau_{av}u_0^{av}(0)$. In addition, one can also conclude that

$$|\bar{\sigma}(t)| \leq \pi_{\omega_a} + \kappa_m\tau_{av}\|u_0^{av}\| + \kappa_m\tau_{av}|u_0^{av}|\,. \tag{4.11}$$

Note that, the more conservative estimate can also be obtained

$$|\bar{\sigma}(t)| \leq \pi_{\omega_a} + 2\kappa_m\tau_{av}\|u_0^{av}\|\,. \tag{4.12}$$

leading to the conclusion that the $\bar{\sigma}$-dynamics is ISS-like w.r.t. u_{av}, with gain $2\kappa_m\tau_{av}$. More precisely, when $u_{av}(0) = 0$, one can conclude that $\omega_a(0) = |\bar{\sigma}(0)|$ and $\pi_{\omega_a} = |\bar{\sigma}(0)|e^{-a_m t}$, consequently, the $\bar{\sigma}$-dynamics is ISS-like w.r.t. u_{av}. When $u_{av}(0) \neq 0$, we can write that $|\sigma_a(0)| \leq |\bar{\sigma}(0)| + \kappa_m\tau_{av}|u_0^{av}(0)|$ and thus $\pi_{\omega_a} \leq \pi_{\bar{\sigma}} + d_{\bar{\sigma}}$, where $\kappa_m\tau_{av}|u_0^{av}(0)|e^{-a_m t} \leq d_{\bar{\sigma}} = \kappa_m\tau_{av}|u_0^{av}(0)|$ and $\pi_{\bar{\sigma}} := |\bar{\sigma}(0)|e^{-a_m t}$, leading to the conclusion that the $\bar{\sigma}$-dynamics is ISpS w.r.t. u_{av} with gain $2\kappa_m\tau_{av}$ satisfying

$$|\bar{\sigma}(t)| \leq \pi_{\bar{\sigma}} + 2\kappa_m\tau_{av}\|u_0^{av}\| + d_{\bar{\sigma}}\,. \tag{4.13}$$

■

4.1 SSC Applied to the Altitude Dynamics

Consider the second order altitude dynamics of the UAV in (3.4), which has relative degree two ($n^* = 2$) from the control input u to the altitude z and can be rewritten[2] as

$$\ddot{z} = k_p(t)u(t) - g\,, \tag{4.14}$$

where $k_p(t) := \frac{1}{\Theta^*(t)} = \frac{k_h(t)k_g(z(t),t)}{m}$ satisfies

$$\underline{k}_p := \frac{k_{g_{min}}k_{h_{min}}}{m} \leq |k_p(t)| \leq \frac{k_{g_{max}}k_{h_{max}}}{m} := \bar{k}_p\,, \tag{4.15}$$

according to **(H1.c)** and **(H2)**. The tracking error dynamics is given by

$$\ddot{e} = k_p[u(t) - g/k_p - \ddot{z}_r/k_p]\,. \tag{4.16}$$

The *ideal output variable* $\sigma = \dot{e} + l_0 e$ satisfies

$$\dot{\sigma} = k_p[-u_0^{av} + U_d]\,, \tag{4.17}$$

where

$$U_d := u_{nom} + \frac{1}{k_p}[-g - \ddot{z}_r + l_0\sigma - l_0^2 e]\,,$$

or, equivalently,

$$U_d := u_{nom} + \frac{1}{k_p}[-g - \ddot{z}_r + l_0\dot{e}]\,.$$

The following realization for (4.3), with $n^* = 2$, can be considered:

$$\tau_f\dot{x}_f = -x_f + e\,, \quad \tau_f\hat{\sigma} = -(1 - \tau_f l_0)x_f + e\,, \tag{4.18}$$

or, equivalently,

$$\tau_f\dot{\hat{\sigma}} = -\hat{\sigma} + \sigma\,.$$

The *ideal sliding variable estimation error* $\tilde{\sigma} := \sigma - \hat{\sigma}$ satisfies

$$\tilde{\sigma} = \tau_f\dot{\hat{\sigma}}$$

and one can also write

$$\tau_f\dot{\tilde{\sigma}} = -\tilde{\sigma} + \tau_f\dot{\sigma}\,.$$

[2]However, it can be applied for a broader class of nonlinear plants with arbitrary relative degree, omitted here for sake of clarity.

From (4.4), (4.5) and (4.17), the $\tilde{\sigma}$-dynamics is given by:

$$\dot{\tilde{\sigma}} = k_p[-u_0^{av} + U_d] - \kappa_m[u_0 - u_0^{av}] + a_m\bar{\sigma}\,. \tag{4.19}$$

For the relative degree one case one has that: $\tau_f = 0$ in (4.3) such that $\hat{\sigma}(t) = \sigma = L(s)e(t)$ and $\tilde{\sigma} = \sigma - \bar{\sigma}$.

For the relative degree two case one has that: $\tau_f \neq 0$ in (4.3) such that $\hat{\sigma}(t) = \frac{L(s)}{F(\tau_f s)}e(t) \neq \sigma = L(s)e(t)$ and $\tilde{\sigma} = \hat{\sigma} - \bar{\sigma}$.

The $\hat{\sigma}$-dynamics can be expressed as:

$$\dot{\hat{\sigma}} \;=\; \begin{cases} k_p[-u_0^{av} + U_d]\,, & n^* = 1\,, \\ \\ \frac{\tilde{\sigma}}{\tau_f}\,, & n^* = 2\,, \end{cases}$$

while the $\tilde{\sigma}$-dynamics can be written as

$$\dot{\tilde{\sigma}} + a_m\tilde{\sigma} \;=\; \begin{cases} k_p[-u_0^{av} + U_d] - \kappa_m[u_0 - u_0^{av}] + a_m\sigma\,, & n^* = 1\,, \\ \\ -\kappa_m[u_0 - u_0^{av}] + a_m\sigma + \left(\frac{1}{\tau_f} - a_m\right)\tilde{\sigma}\,, & n^* = 2\,. \end{cases}$$

4.2 The Relative Degree One Case

For sake of simplicity, we focus here on the relative degree one case, i.e., when $\dot{z}$ is measured. It is a very usual case considering UAV control applications. The case when $\dot{z}$ is not available can be covered by SSC scheme for arbitrary relative degree n^*, in particular for $n^* = 2$ when the UAV altitude dynamics is considered.

When the *ideal output variable* is available for feedback we can set $\tau_f = 0$ in (4.3) so that $\hat{\sigma}(t) = \sigma = L(s)e(t)$ and the sliding variable $\tilde{\sigma}$ becomes,

$$\tilde{\sigma} := \sigma - \bar{\sigma}\,. \tag{4.20}$$

From (4.20), (4.17) and (4.5) the $\tilde{\sigma}$-dynamics is given by:

$$\dot{\tilde{\sigma}} = k_p[-u_0^{av} + U_d] - \kappa_m[u_0 - u_0^{av}] + a_m\bar{\sigma}\,, \tag{4.21}$$

or, equivalently,

$$\dot{\tilde{\sigma}} + a_m\tilde{\sigma} = k_p[-u_0^{av} + U_d] - \kappa_m[u_0 - u_0^{av}] + a_m\sigma\,. \tag{4.22}$$

Equivalent Control and Reduced Dynamics

The realization of the ideal sliding modes are important to ensure robustness

and chattering alleviated smooth control signal. In *SSC*, an ideal sliding surface is given by $\tilde{\sigma}(t) \equiv 0$.

If ideal sliding occurs $\tilde{\sigma}(t) \equiv 0$ the *equivalent control* u_{eq} is given by

$$u_{eq} = u_0^{av} + \frac{k_p}{\kappa_m}[-u_0^{av} + U_d] + \frac{a_m}{\kappa_m}\sigma\,, \tag{4.23}$$

resulting in the following *reduced dynamics*:

$$\tau_{av}\dot{u}_0^{av} = -\frac{k_p}{\kappa_m}u_0^{av} + \frac{k_p}{\kappa_m}U_d + \frac{a_m}{\kappa_m}\sigma\,. \tag{4.24}$$

Remark 2 *(***Similarity with the Integral Sliding Mode Control***) It must be highlighted that the plant nonlinearities affects the system via the time varying high frequency gain $k_p(t)$. Moreover, despite of a filtered version of the VSC law be in fact applied to the plant input, we guarantee that no VSC robustness is lost, similarly to the Integral Sliding Mode control scheme proposed by [26]. The robustness is regarded w.r.t. the sliding mode which occurs in the sliding surface $\tilde{\sigma} \equiv 0$, corresponding to an internal control loop (the prediction error loop).*

Remark 3 *(***Control Action During Sliding Mode***) One can verify that the SSC control law approaches a PI control.* ∎

4.2.1 Boundedness and Convergence of $\tilde{\sigma}$

Putting together the $\tilde{\sigma}$-dynamics (4.22) and the averaging filter dynamics the following 2-th order system results:

$$\tau_{av}\dot{u}_0^{av} = -u_0^{av} + u_0\,, \tag{4.25}$$

$$\dot{\tilde{\sigma}} + a_m\tilde{\sigma} = k_p[-u_0^{av} + U_d] - \kappa_m[u_0 - u_0^{av}] + a_m\sigma\,. \tag{4.26}$$

Inspired by the reduced dynamics during sliding mode (4.24), define the following auxiliary dynamics:

$$\tau_{av}\dot{\eta}_1 = \frac{k_p}{\kappa_m}[-\eta_1 + U_d] + \frac{a_m}{\kappa_m}\sigma\,. \tag{4.27}$$

Now, by using the change of coordinates

$$\tilde{x}_1 := u_0^{av} - \eta_1\,,$$

it is possible to obtain the following closed-loop dynamics:

$$\tau_{av}\dot{\tilde{x}}_1 = -\tilde{x}_1 + [u_0 + d_{eq2}]\,, \tag{4.28}$$

$$\dot{\tilde{\sigma}} = -a_m\tilde{\sigma} + (\kappa_m - k_p)\tilde{x}_1 - \kappa_m[u_0 + d_{eq2}]\,, \tag{4.29}$$

where the *equivalent input disturbance* d_{eq2} is defined as

$$d_{eq2} := -\eta_1 + \frac{k_p}{\kappa_m}\eta_1 - \frac{k_p}{\kappa_m}U_d - \frac{a_m}{\kappa_m}\sigma\,. \tag{4.30}$$

Letting

$$\tilde{x} := \begin{bmatrix} \tilde{x}_1 & \tilde{\sigma} \end{bmatrix}^T\,, \tag{4.31}$$

from (4.28) and (4.29), one can write:

$$\dot{\tilde{x}} = A_e(t)\tilde{x} + B_e[u_0 + d_{eq2}]\,, \quad \tilde{\sigma} = C_e\tilde{x}\,, \tag{4.32}$$

where

$$A_e(t) := \begin{bmatrix} -1/\tau_{av} & 0 \\ \kappa_m - k_p(t) & -a_m \end{bmatrix}\,,$$

$B_e := \begin{bmatrix} 1/\tau_{av} & -\kappa_m \end{bmatrix}^T$ and $C_e := \begin{bmatrix} 0 & 1 \end{bmatrix}$. Moreover, by adding and subtracting $B_e k_0\tilde{\sigma} = B_e C_e k_0\tilde{x}$, one can write

$$\dot{\tilde{x}} = \bar{A}_e(t)\tilde{x} + B_e[u_0 + d_{eq2} - k_0\tilde{\sigma}]\,, \quad \tilde{\sigma} = C_e\tilde{x}\,, \tag{4.33}$$

where

$$\bar{A}_e(t) := A_e(t) + B_e C_e k_0 = \begin{bmatrix} -1/\tau_{av} & k_0/\tau_{av} \\ \kappa_m - k_p(t) & -a_m - k_0\kappa_m \end{bmatrix}\,.$$

The following lemma can now be demonstrated.

Lemma 4 *Consider the dynamic (4.33), with control u_0 given in (4.8) and equivalent input disturbance $d_{eq2}(t)$ in (4.30). If the modulation function in (4.8) satisfies $\varrho = \bar{\varrho} + k_0|\tilde{\sigma}|$ with*

$$\bar{\varrho}(t) \geq |d_{eq2}(t)| + \delta\,, \quad \forall t \in [0, t_M)\,, \tag{4.34}$$

modulo *vanishing terms, $\delta \geq 0$ been an arbitrary constant and $k_0 > 0$ a design constant, then the inequality*

$$|\tilde{\sigma}(t)|\,, |\tilde{x}| \leq \pi_{\tilde{\sigma}}\,, \quad \forall t \in [0, t_M)\,, \tag{4.35}$$

holds, where $\pi_{\tilde{\sigma}} := k_{\tilde{\sigma}}|\tilde{x}(0)|e^{-\lambda_{\tilde{\sigma}}t}$, $k_{\tilde{\sigma}} > 0$ and $0 < \lambda_{\tilde{\sigma}}$ are appropriate constants.

Proof: See Appendix A.

When $k_p(t)$ is a **constant**, the system (A_e, B_e, C_e) is ASPR (Almost Strictly Positive Real). Indeed, since $C_e B_e = -\kappa_m \neq 0$, then (A_e, B_e, C_e) has relative degree one. Moreover, by using the Rosenbrock system matrix, the triple (A_e, B_e, C_e) is minimum phase, since there exists a zero at $-k_p/(\kappa_m \tau_{av})$. Thus, for a large enough $k_0 > 0$, $(\bar{A}_e, B_e, C_e)$ is SPR. Then, the proof follows the steps in [27].

For a **time varying** $k_p(t)$, one can also obtain a similar conclusion but the proof is more involved. First, choose the Lyapunov function $\tilde{V} := \tilde{x}^T P \tilde{x}$ with $P = P^T = \begin{bmatrix} \tau_{av}\kappa_m & 1 \\ 1 & \frac{\tau_{av}+1}{\tau_{av}\kappa_m} \end{bmatrix} > 0$. Then, one can verify that $\bar{A}_e^T(t)P + P\bar{A}_e(t) := -Q(t) < 0$, $\forall t \in [0, t_M)$, for a sufficiently large k_0.

It is clear that there exists $\lambda > 0$ such that

$$-\tilde{x}^T Q \tilde{x} \leq -\lambda[\tilde{x}_1^2 + \tilde{x}_2^2] = -\lambda|\tilde{x}|^2 \,,$$

where one obvious choice is $\lambda = \lambda_m(Q)$. However, an alternative choice is given later on. The time derivative of $\tilde{V}$ along the solutions of (4.33) is given by

$$\dot{\tilde{V}} = -\tilde{x}^T Q \tilde{x} + 2\tilde{x}^T P B_e [u_0 + d_{eq2} - k_0 \tilde{\sigma}] \,,$$

or,

$$\dot{\tilde{V}} = -\tilde{x}^T Q \tilde{x} - 2\tilde{\sigma} [u_0 + d_{eq2} - k_0 \tilde{\sigma}] \,,$$

since one can verify that $PB_e = -C_e^T$. Therefore,

$$\dot{\tilde{V}} \leq -\lambda|\tilde{x}|^2 + 2|\tilde{\sigma}|[-\bar{\varrho} + |d_{eq2}|] \,,$$

where the relationship

$$\varrho = \bar{\varrho} + k_0|\tilde{\sigma}| \,,$$

was used. Now, if $\bar{\varrho}(t) \geq |d_{eq2}(t)| + \delta$, then

$$\dot{\tilde{V}} \leq -\lambda|\tilde{x}|^2 - 2|\tilde{\sigma}|\delta < -\lambda|\tilde{x}|^2 \leq -\frac{\lambda}{\lambda_m(P)}\tilde{V} \,.$$

By the using the Comparison Lemma with discontinuous right-side, Theorem 8 in [17], one has that

$$|\tilde{\sigma}| \leq |\tilde{x}| \leq \sqrt{\frac{\lambda_M(P)}{\lambda_m(P)}} e^{-\frac{\lambda}{2\lambda_M(P)}t} |\tilde{x}(0)| \,.$$

One possible choice for λ is given in what follows. First, one can verify that

$$q_{22} = 2a_m \frac{\tau_{av}+1}{\kappa_m \tau_{av}} + 2k_0 > 0 \,,$$

$$q_{12} = q_{21} = \frac{-\kappa_m \tau_{av} + k_p(t) + \tau_{av} k_p(t) + a_m \kappa_m \tau_{av}}{\kappa_m \tau_{av}},$$

and

$$q_{11} = 2k_p(t) > 0\,,$$

where q_{ij} are the elements of the matrix Q and $-\tilde{x}^T Q \tilde{x} = -q_{11}\tilde{x}_1^2 - q_{22}\tilde{x}_2^2 - 2q_{12}\tilde{x}_1\tilde{x}_2$, where $q_{11}, q_{22} > 0$.

By noting that $|\tilde{x}_1||\tilde{x}_2| \leq \frac{1}{4a^2}\tilde{x}_1^2 + a^2\tilde{x}_2^2$, for any real $a > 0$, then one can conclude that $-\tilde{x}^T Q \tilde{x} \leq -q_{22}\tilde{x}_1^2 - q_{11}\tilde{x}_2^2 + 2|q_{12}|\frac{1}{4a^2}\tilde{x}_1^2 + 2|q_{12}|a^2\tilde{x}_2^2$. Hence,

$$-\tilde{x}^T Q \tilde{x} \leq -\left[q_{22} - 2|q_{12}|\frac{1}{4a^2}\right]\tilde{x}_1^2 - \left[q_{11} - 2|q_{12}|a^2\right]\tilde{x}_2^2\,.$$

Now, if we choose $a^2 < (q_{11} - \lambda)/(2|q_{12}|)$ and $q_{22} > \lambda + 2|q_{12}|\frac{1}{4a^2}$ then one has

$$-\tilde{x}^T Q \tilde{x} \leq -\lambda[\tilde{x}_1^2 + \tilde{x}_2^2] = -\lambda|\tilde{x}|^2\,,$$

for any λ such that $q_{11} > \lambda > 0$. ∎

4.2.2 Modulation Function Implementation

For the modulation function implementation, considering the relative degree one case, all the signals $\ddot{z}_r, \dot{e}, e, \sigma$ and u_{nom} are available. Moreover, the constant g is known (but just an upper bound is really needed). Thus, recalling that the disturbance U_d is given by

$$U_d := u_{nom} + \frac{1}{k_p}[-g - \ddot{z}_r + l_0\dot{e}]\,,$$

then the following norm bounds hold

$$|U_d| \leq |u_{nom}| + \frac{1}{\underline{k}_p}\omega_1 := \omega_2\,.$$

$$|k_p U_d| \leq \bar{k}_p|u_{nom}| + \omega_1 := \omega_3\,.$$

where $\omega_1 := |-g - \ddot{z}_r + l_0\dot{e}|$, ω_2 and ω_3 are available signals. Hence, the term $-\frac{k_p}{\kappa_m}U_d - \frac{a_m}{\kappa_m}\sigma$ appearing in both disturbances d_{eq1} and d_{eq2} satisfies

$$\left|-\frac{k_p}{\kappa_m}U_d - \frac{a_m}{\kappa_m}\sigma\right| \leq \frac{1}{\kappa_m}\omega_3 + \frac{a_m}{\kappa_m}|\sigma| := \omega_4\,,$$

where ω_4 is an available signal.

A norm observer for η_1-dynamics (4.27), repeated in what follows for convenience,

is needed:

$$\tau_{av}\dot{\eta}_1 = -\frac{k_p}{\kappa_m}\eta_1 + \frac{k_p}{\kappa_m}U_d + \frac{a_m}{\kappa_m}\sigma\,. \tag{4.36}$$

By applying Lemma 11 to (4.36) one has that the dynamics

$$\tau_{av}\dot{\omega}_5 = -\frac{k_p}{\kappa_m}\omega_5 + \omega_4\,,$$

with $\omega_5(0) = W_1(0) = |\eta_1(0)| = |u_0^{av}(0)|$ is a norm observer for (4.36), since

$$\left|\frac{k_p}{\kappa_m}U_d + \frac{a_m}{\kappa_m}\sigma\right| \leq \omega_4\,.$$

Moreover, the following inequality holds

$$|\eta_1| \leq \omega_5\,.$$

The *equivalent input disturbance*

$$d_{eq2} := -\eta_1 + \frac{k_p}{\kappa_m}\eta_1 - \frac{k_p}{\kappa_m}U_d - \frac{a_m}{\kappa_m}\sigma\,, \tag{4.37}$$

can now be norm bounded by

$$|d_{eq2}| \leq (1 + \frac{\bar{k}_p}{\kappa_m})\omega_5 + \omega_4\,, \tag{4.38}$$

so that the modulation function can be designed as

$$\bar{\rho} := (1 + \frac{\bar{k}_p}{\kappa_m})\omega_5 + \omega_4 + \delta\,. \tag{4.39}$$

In this case, the modulation function is given by the output of the following dynamics system

$$\tau_{av}\dot{\omega}_5 = -\frac{k_p}{\kappa_m}\omega_5 + \omega_4\,, \tag{4.40}$$

$$\varrho = (1 + \frac{\bar{k}_p}{\kappa_m})\omega_5 + \omega_4 + \delta + k_0|\tilde{\sigma}|\,, \tag{4.41}$$

with $\omega_5(0) = u_0^{av}(0)$ and ω_4 (available) being given by

$$\omega_4 = \frac{1}{\kappa_m}(\bar{k}_p|u_{nom}| + \omega_1) + \frac{a_m}{\kappa_m}|\sigma|\,, \tag{4.42}$$

$$\omega_1 = |-g - \ddot{z}_r - l_0^2 e + l_0\sigma|\,. \tag{4.43}$$

Note that, (4.40) is an open-loop strictly stable system with output (4.41) and ω_4 and $\tilde{\sigma}$ being treated as exogenous available signals. Thus, from (4.40)–(4.43), the modulation function is uniformly bounded as long as u_{nom}, $\ddot{z}_r$, e, σ and $\tilde{\sigma}$ are uniformly norm bounded.

4.2.3 Closed-Loop Convergence Analysis

The *tracking error convergence* property is stated in the following theorem.

Theorem 5 *Assume that the velocity $\dot{z}$ is available and (***H1***)–(***H3***) hold. Consider the plant (3.4) with output tracking error (4.1), SSC control law (4.6), (4.7), (4.8) with sliding variable $\tilde{\sigma}$ in (4.20), prediction error (4.5) and modulation function $\varrho = \bar{\varrho} + k_0|\tilde{\sigma}|$, with $\bar{\varrho}$ in (4.39) satisfying (4.34) and k_0 being an appropriate constant. The desired trajectory to be followed is described in (3.6). Then, for sufficiently small time constant of the smooth filter (τ_{av}) in (4.7), the tracking error converges to a small residual set of order $\mathcal{O}(\tau_{av})$ and the following inequality holds*

$$|e(t)| \leq \mathcal{O}(\tau_{av}) + \pi_e \,, \tag{4.44}$$

where π_e is a vanishing term depending on the initial conditions and this residual set does not depend on the initial conditions. In addition, all closed-loop signals remain uniformly bounded.

Proof: See Appendix A. Since u_{nom} satisfies **(H3)** and $\ddot{z}_r$ are assumed norm bounded and recalling that

$$\dot{e} = -l_0 e + \sigma \,,$$

one can conclude from (4.40)–(4.43) and Lemma 11 that the ω_5-dynamics (4.40) is ISpS w.r.t. σ and $\tilde{\sigma}$, with ISpS gain *independent* of τ_{av}. Consequently, from (4.41) the modulation function satisfies

$$\|\varrho\| \leq k_\rho \|\sigma\| + k_{\tilde{\sigma}} |\tilde{\sigma}| + \pi_\rho \,,$$

where k_ρ, $k_{\tilde{\sigma}} > 0$ is an appropriate constant (independent of the initial conditions and τ_{av}) and π_ρ is an exponentially decaying term depending on the initial conditions $|u_0^{av}(0)|$ and $|e(0)|$.

In addition, recalling that $\sigma = \bar{\sigma} + \tilde{\sigma}$ and using Lemmas 1 and 8, one has that

$$\|\sigma\| \leq k_\sigma \tau_{av} \|u_0^{av}\| + \pi_\sigma \,.$$

where $k_\sigma > 0$ is an appropriate constant (independent of the initial conditions and τ_{av}) and π_σ is an exponentially decaying term depending on the initial conditions

$|u_0^{av}(0)|$, $|\bar{\sigma}(0)|$ and $|e(0)|$ and $|\dot{e}(0)|$. Therefore, one can write

$$\|\varrho\| \leq k_\rho k_\sigma \tau_{av} \|u_0^{av}\| + \pi_\varrho \,,$$

where π_ϱ is an exponentially decaying term depending on the initial conditions $|u_0^{av}(0)|$, $|\bar{\sigma}(0)|$ and $|e(0)|$ and $|\dot{e}(0)|$, which satisfies $k_\rho \pi_\sigma + k_0 |\tilde{\sigma}| + \pi_\rho < \pi_\varrho$. Now, applying the Small Gain Theorem to

$$\tau_{av} \dot{u}_0^{av} = -u_0^{av} + \varrho(t) \mathrm{sgn}(\tilde{\sigma}) \,,$$

one can conclude, for sufficiently small τ_{av}, that u_0^{av} is uniformly norm bounded by a constant independent of the initial conditions and τ_{av}.

Moreover, one can subsequently conclude that, ϱ, $\bar{\sigma}$ (Lemma 1), $\sigma = \bar{\sigma} + \tilde{\sigma}$, e (the e-dynamics $\dot{e} = -l_0 e + \sigma$ is ISS w.r.t. σ) and $\dot{e} = -l_0 e + \sigma$ are all uniformly norm bounded ($t_M \to +\infty$). In addition, the signals $\bar{\sigma}$, σ and e converge to a residual set of order $\mathcal{O}(\tau_{av})$ and, in particular, the following inequality holds

$$|e(t)| \leq \mathcal{O}(\tau_{av}) + \pi_e \,,$$

where π_e is a vanishing term depending on the initial conditions and this residual set does not depend on the initial conditions. ∎

4.2.4 Existence of Ideal Sliding Mode

As mentioned before, the realization of the ideal sliding modes are important to ensure that *chattering* is avoided. In the *SSC*, an ideal sliding surface is given by $\tilde{\sigma}(t) \equiv 0$.

From (4.29), the $\tilde{\sigma}$-dynamics satisfies

$$\dot{\tilde{\sigma}} \;=\; -a_m \tilde{\sigma} + (\kappa_m - k_p)\tilde{x}_1 - \kappa_m [u_0 + d_{eq2}] \,, \tag{4.45}$$

or,

$$\dot{\tilde{\sigma}} \;=\; -a_m \tilde{\sigma} - \kappa_m \left[u_0 + d_{eq2} - \frac{(\kappa_m - k_p)}{\kappa_m} \tilde{x}_1 \right] . \tag{4.46}$$

Hence, one has that

$$\dot{\tilde{\sigma}} \tilde{\sigma} = -a_m \tilde{\sigma}^2 - \kappa_m \left[\tilde{\sigma} u_0 + \tilde{\sigma} d_{eq2} - \tilde{\sigma} \frac{(\kappa_m - k_p)}{\kappa_m} \tilde{x}_1 \right] ,$$

and, since $\tilde{\sigma}u_0 = (\bar{\varrho} + k_0|\tilde{\sigma}|)\tilde{\sigma}\text{sgn}(\tilde{\sigma}) = \bar{\varrho}|\tilde{\sigma}| + k_0\tilde{\sigma}^2$. Therefore, one has

$$\dot{\tilde{\sigma}}\tilde{\sigma} = -a_m\tilde{\sigma}^2 - \kappa_m k_0\tilde{\sigma}^2 + \kappa_m\left[-\bar{\varrho}|\tilde{\sigma}| - \tilde{\sigma}d_{eq2} + \tilde{\sigma}\frac{(\kappa_m - k_p)}{\kappa_m}\tilde{x}_1\right],$$

and leading to the following upper bound

$$\dot{\tilde{\sigma}}\tilde{\sigma} \leq \kappa_m\left[-\bar{\varrho} + |d_{eq2}| + \left|\frac{(\kappa_m - k_p)}{\kappa_m}\right||\tilde{x}_1|\right]|\tilde{\sigma}|\,.$$

Finally, from Lemma 8, $\tilde{x}_1$ satisfying

$$|\tilde{x}_1| \leq |\tilde{x}| \leq \pi_{\tilde{\sigma}}\,, \quad \forall t \in [0, +\infty)\,, \tag{4.47}$$

assures that there exists $t_s > 0$ such that $\left|\frac{(\kappa_m - k_p)}{\kappa_m}\right||\tilde{x}_1(t)| \leq \delta_1$, $\forall t \geq t_s$ and for any $\delta_1 > 0$. Hence, since the modulation function is designed for satisfying $\bar{\varrho} > |d_{eq2}| + \delta$, with $\delta > \delta_1$, one can conclude that

$$\dot{\tilde{\sigma}}\tilde{\sigma} \leq -\kappa_m\left[\delta - \delta_1\right]|\tilde{\sigma}|\,,$$

leading to the conclusion that there exists a finite time $t_e \geq 0$ such that $\tilde{\sigma}(t)$ becomes identically zero $\forall t \geq t_e$.

4.2.5 Extra Case

Boundedness and Convergence of $\tilde{\sigma}$: Extra Case

From (4.22) the $\tilde{\sigma}$-dynamics can be rewritten as:

$$\dot{\tilde{\sigma}} = -a_m\tilde{\sigma} - \kappa_m[u_0 + d_{eq1}]\,, \tag{4.48}$$

where the *equivalent input disturbance* d_{eq1} is defined as

$$d_{eq1} := -u_0^{av} + \frac{k_p}{\kappa_m}u_0^{av} - \frac{k_p}{\kappa_m}U_d - \frac{a_m}{\kappa_m}\sigma\,. \tag{4.49}$$

The following lemma can now be demonstrated.

Lemma 6 *Consider the dynamic (4.48), with control u_0 given in (4.8) and equivalent input disturbance $d_{eq1}(t)$ in (4.49). If the modulation function in (4.8) satisfies*

$$\varrho(t) \geq |d_{eq1}(t)| + \delta\,, \quad \forall t \in [0, t_M)\,, \tag{4.50}$$

modulo *vanishing terms, $\delta \geq 0$ been an arbitrary constant and $k_0 > 0$ a design*

constant, then the inequality

$$|\tilde{\sigma}(t)| \leq \pi_{\tilde{\sigma}}\,, \quad \forall t \in [0, t_M)\,, \tag{4.51}$$

holds, where $\pi_{\tilde{\sigma}} := k_{\tilde{\sigma}}|\tilde{x}(0)|e^{-\lambda_{\tilde{\sigma}}t}$, $k_{\tilde{\sigma}} > 0$ *and* $0 < \lambda_{\tilde{\sigma}}$ *are appropriate constants.*

Proof: See Appendix A.

Modulation Function: Extra Case

A norm bound for the disturbance

$$d_{eq1} := -u_0^{av} + \frac{k_p}{\kappa_m}u_0^{av} - \frac{k_p}{\kappa_m}U_d - \frac{a_m}{\kappa_m}\sigma\,, \tag{4.52}$$

can be directly obtained as

$$d_{eq1} \leq |u_0^{av}| + \frac{\bar{k}_p}{\kappa_m}|u_0^{av}| + \omega_4\,, \tag{4.53}$$

so that the modulation function can be designed as

$$\varrho := |u_0^{av}| + \frac{\bar{k}_p}{\kappa_m}|u_0^{av}| + \omega_4 + \delta\,. \tag{4.54}$$

In this case, the modulation function is thus given by the output of the following dynamics system

$$\begin{aligned} \tau_{av}\dot{u}_0^{av} &= -u_0^{av} + \varrho(t)\mathrm{sgn}(\tilde{\sigma})\,, & (4.55)\\ \varrho &= |u_0^{av}| + \frac{\bar{k}_p}{\kappa_m}|u_0^{av}| + \omega_4 + \delta\,. & (4.56) \end{aligned}$$

with $\omega_4 = \frac{1}{\kappa_m}(\bar{k}_p|u_{nom}| + |-g - \ddot{z}_r + l_0\dot{e}|) + \frac{a_m}{\kappa_m}|\sigma|$. Note that, (4.55) and (4.56) is a closed loop system with ω_4 and $\tilde{\sigma}$ being exogenous available signals. Thus, stability must be assessed.

Closed-Loop Convergence Analysis and Existence of Ideal Sliding Mode: Extra Case

Both was left for future work.

4.3 The Relative Degree Two Case

When $\dot{z}$ is not available for feedback, the *ideal output variable* is not available for feedback and we have to use the surrogate (4.3) instead.

For the relative degree two case one has that: $\tau_f \neq 0$ in (4.3) so that $\hat{\sigma}(t) = \frac{L(s)}{F(\tau_f s)} e(t) \neq \sigma = L(s)e(t)$ and $\tilde{\sigma} = \hat{\sigma} - \bar{\sigma}$.

The $\hat{\sigma}$-dynamics can be expressed as:

$$\dot{\hat{\sigma}} = \frac{\tilde{\sigma}}{\tau_f}\,, \tag{4.57}$$

while the $\tilde{\sigma}$-dynamics can be written as

$$\dot{\tilde{\sigma}} + a_m \tilde{\sigma} = -\kappa_m [u_0 - u_0^{av}] + a_m \hat{\sigma} + \tilde{\sigma}/\tau_f\,. \tag{4.58}$$

Equivalent Control and Reduced Dynamics

If ideal sliding occurs $\tilde{\sigma}(t) \equiv 0$ the *equivalent control* u_{eq} is given by

$$u_{eq} \;=\; u_0^{av} + \frac{1}{\tau_f \kappa_m}\tilde{\sigma} + \frac{a_m}{\kappa_m}\hat{\sigma}\,, \tag{4.59}$$

resulting in the following *reduced dynamics*:

$$\begin{aligned}
\tau_{av}\dot{u}_0^{av} &= \frac{1}{\tau_f \kappa_m}\tilde{\sigma} + \frac{a_m}{\kappa_m}\hat{\sigma}\,, && (4.60)\\
\tau_f \dot{\tilde{\sigma}} &= -\tau_f k_p u_0^{av} + (l_0\tau_f - 1)\tilde{\sigma} + \tau_f l_0 \hat{\sigma} + \tau_f k_p D\,, && (4.61)\\
\tau_f \dot{\hat{\sigma}} &= \tilde{\sigma}\,, && (4.62)
\end{aligned}$$

where

$$D := U_d - \frac{l_0}{k_p}(\hat{\sigma} + \tilde{\sigma}) = u_{nom} + \frac{1}{k_p}[-g - \ddot{z}_r - l_0^2 e]\,.$$

Remark 7 *(***Control Action During Sliding Mode***) One can verify that the SSC control law approaches a PI control.* ∎

4.3.1 Boundedness and Convergence of $\tilde{\sigma}$

Putting together the $\tilde{\sigma}$-dynamics (4.58), the $\tilde{\sigma}$-dynamics and the averaging filter dynamics and the $\hat{\sigma}$-dynamics, the following 4-th order system results:

$$\begin{aligned}
\tau_{av}\dot{u}_0^{av} &= -u_0^{av} + u_0\,, && (4.63)\\
\tau_f \dot{\tilde{\sigma}} &= -\tau_f k_p u_0^{av} + (l_0\tau_f - 1)\tilde{\sigma} + \tau_f l_0 \hat{\sigma} + \tau_f k_p D\,, && (4.64)\\
\tau_f \dot{\hat{\sigma}} &= \tilde{\sigma}\,, && (4.65)\\
\dot{\tilde{\sigma}} + a_m\tilde{\sigma} &= -\kappa_m[u_0 - u_0^{av}] + a_m\hat{\sigma} + \tilde{\sigma}/\tau_f\,, && (4.66)
\end{aligned}$$

Inspired by the reduced dynamics during sliding mode (4.60)–(4.62), define the following auxiliary dynamics:

$$\begin{aligned}
\tau_{av}\dot{\eta}_1 &= \frac{1}{\kappa_m}\eta_2 + \frac{a_m}{\kappa_m}\eta_3\,, && (4.67)\\
\tau_f\dot{\eta}_2 &= -k_p\eta_1 + (l_0\tau_f - 1)\eta_2 + l_0\eta_3 + k_pD\,, && (4.68)\\
\dot{\eta}_3 &= \eta_2\,, && (4.69)
\end{aligned}$$

Now, by using the change of coordinates

$$\tilde{x}_1 := u_0^{av} - \eta_1\,, \quad \tilde{x}_2 := \tilde{\sigma} - \tau_f\eta_2\,, \quad \tilde{x}_3 := \hat{\sigma} - \eta_3$$

it is possible to obtain the following closed-loop dynamics:

$$\begin{aligned}
\tau_{av}\dot{\tilde{x}}_1 &= -\tilde{x}_1 + [u_0 + d_{eq3}]\,, && (4.70)\\
\tau_f\dot{\tilde{x}}_2 &= -\tau_f k_p\tilde{x}_1 + (l_0\tau_f - 1)\tilde{x}_2 + \tau_f l_0\tilde{x}_3\,, && (4.71)\\
\tau_f\dot{\tilde{x}}_3 &= \tilde{x}_2\,, && (4.72)\\
\dot{\tilde{\sigma}} + a_m\tilde{\sigma} &= \kappa_m\tilde{x}_1 + \frac{1}{\tau_f}\tilde{x}_2 + a_m\tilde{x}_3 - \kappa_m[u_0 + d_{eq3}]\,, && (4.73)
\end{aligned}$$

where the *equivalent input disturbance* d_{eq3} is defined as

$$d_{eq3} := \eta_1 + \frac{1}{\kappa_m}\eta_2 + \frac{a_m}{\kappa_m}\eta_3\,. \qquad (4.74)$$

Letting

$$\tilde{x} := \left[\begin{array}{cccc} \tilde{x}_1 & \tilde{x}_2 & \tilde{x}_2 & \tilde{\sigma} \end{array}\right]^T\,,, \qquad (4.75)$$

one can write:

$$\dot{\tilde{x}} = A_e(t)\tilde{x} + B_e[-u_0 + d_{eq3}]\,, \quad \tilde{\sigma} = C_e\tilde{x}\,, \qquad (4.76)$$

where

$$A_e(t) := \left[\begin{array}{cccc} -1/\tau_{av} & 0 & 0 & 0 \\ -k_p & (l_0\tau_f - 1)/\tau_f & l_0 & 0 \\ 0 & \frac{1}{\tau_f} & 0 & 0 \\ \kappa_m & \frac{1}{\tau_f} & a_m & -a_m \end{array}\right],$$

$B_e := \left[\begin{array}{cccc} -1/\tau_{av} & 0 & 0 & \kappa_m \end{array}\right]^T$ and $C_e := \left[\begin{array}{cccc} 0 & 0 & 0 & 1 \end{array}\right]$.

The following lemma can now be demonstrated.

Lemma 8 *Consider the dynamic (4.79), with control u_0 given in (4.8) and equivalent input disturbance $d_{eq3}(t)$ in (4.74). If the modulation function in (4.8) satisfies $\varrho = \bar{\varrho} + k_0|\tilde{\sigma}|$ with*

$$\bar{\varrho}(t) \geq |d_{eq3}(t)| + \delta\,, \quad \forall t \in [0, t_M)\,, \qquad (4.77)$$

modulo *vanishing terms, $\delta \geq 0$ being an arbitrary constant and $k_0 > 0$ a design constant, then the inequality*

$$|\tilde{\sigma}(t)|\,, |\tilde{x}| \leq \pi_{\tilde{\sigma}}\,, \quad \forall t \in [0, t_M)\,, \tag{4.78}$$

holds, where $\pi_{\tilde{\sigma}} := k_{\tilde{\sigma}}|\tilde{x}(0)|e^{-\lambda_{\tilde{\sigma}}t}$, $k_{\tilde{\sigma}} > 0$ and $0 < \lambda_{\tilde{\sigma}}$ are appropriate constants.

Proof: See Appendix A.

When $k_p(t) = k_p^{nom}$ is a **constant**, $A_e(t) = A_e$ is a constant matrix and the system (A_e, B_e, C_e) is ASPR (Almost Strictly Positive Real) for τ_{av} and τ_f small enough. Indeed, since $C_eB_e = \kappa_m \neq 0$, then (A_e, B_e, C_e) has relative degree one. Moreover, by using the Rosenbrock system matrix and the Routh-Hurwitz stability criterion, the triple (A_e, B_e, C_e) is minimum phase, when $\tau_f l_0 < 1$, $\tau_{av}\kappa_m l_0 < k_p^{nom}$ and

$$\tau_{av}\kappa_m l_0(1 - \tau_f l_0) + \tau_f k_p^{nom}(a_m + l_0) < k_p^{nom}\,.$$

Those conditions are satisfied if we choose τ_{av}, τ_f small enough so that $N\tau_{av}\kappa_m l_0 < k_p^{nom}$ and $N\tau_f(a_m + l_0\frac{N-1}{N}) < N - 1$, for any $N > 1$.

Let z_1, z_2, z_3 be the transmission zeros of (A_e, B_e, C_e) and $\lambda_i = \mathcal{R}(z_i) < 0$ be the real part of z_i $(i = 1, 2, 3)$, which is negative since (A_e, B_e, C_e) is minimum phase for τ_{av}, τ_f small enough, as explained above. Moreover, by letting $0 < \lambda_z < -max\{\lambda_1, \lambda_2, \lambda_3\}$, the system $([A_e + \lambda_z I], B_e, C_e)$ has also stable transmission zeros as system (A_e, B_e, C_e).

Indeed, by using the Rosenbrock system matrix one has the transmission zeros of the system $([A_e + \lambda_z I], B_e, C_e)$ are the values of z such that

$$\text{rank}\left\{\begin{bmatrix} (z - \lambda_z)I - A_e & B_e \\ -C_e & 0 \end{bmatrix}\right\} < 4\,,$$

while a transmission zero of the system (A_e, B_e, C_e) is a number z_i such that

$$\text{rank}\left\{\begin{bmatrix} z_i I - A_e & B_e \\ -C_e & 0 \end{bmatrix}\right\} < 4\,.$$

Hence, all zeros of $([A_e + \lambda_z I], B_e, C_e)$ present negative real parts when $0 < \lambda_z < -max\{\lambda_1, \lambda_2, \lambda_3\}$ and thus $([A_e + \lambda_z I], B_e, C_e)$ is also ASPR.

In fact, we can go further and obtain a matrix $P = P^T > 0$ and a feedback gain k_0, such that $(\bar{A}_e, B_e, C_e)$ is SPR, with $\bar{A}_e := A_e + \lambda_z I - B_eC_ek_0$.

The following choice for P assures that $(\bar{A}_e, B_e, C_e)$ is SPR:

$$P = C_e^T(B_e^TC_e^T)^{-1}C_e + B_\perp X B_\perp^T\,,$$

where $B_\perp = \mathcal{N}(B_e^T)$ is the orthogonal null space of B_e and satisfies $B_\perp^T B_e = 0$, $[B_e\ B_\perp]$ is invertible and $B_\perp^T B_\perp = I$, and X is the solution of the following LMI:

$$C_\perp^T \frac{\left(B_\perp X B_\perp^T \bar{A}_e + (B_\perp X B_\perp^T \bar{A}_e)^T\right)}{2} C_\perp < 0\,,$$

with $C_\perp = \mathcal{N}(C_e)$ being the orthogonal null space of C_e^T which satisfies $C_\perp^T C_e^T = 0$, $[C_e^T\ C_\perp]$ be invertible and $C_\perp^T C_\perp = I$. Moreover, the feedback gain k_0 is given by

$$k_0 = C^\dagger H(I - C_\perp (C_\perp^T H C_\perp)^{-1} C_\perp^T H) C^{\dagger T} + k_1\,,$$

where

$$H := (P\bar{A}_e + (P\bar{A}_e)^T)/2\,,$$

and $k_1 > 0$ is an arbitrary constant. In addition, one can verify that P must have the topology

$$P = \begin{bmatrix} \tau_{av}\kappa_m\alpha_1 & \tau_{av}\kappa_m\alpha_2 & \tau_{av}\kappa_m\alpha_3 & \alpha_1 \\ \tau_{av}\kappa_m\alpha_2 & \alpha_5 & \alpha_4 & \alpha_2 \\ \tau_{av}\kappa_m\alpha_3 & \alpha_4 & \alpha_6 & \alpha_3 \\ \alpha_1 & \alpha_2 & \alpha_3 & \frac{\tau_{av}+\alpha_1}{\tau_{av}\kappa_m} \end{bmatrix}$$

to satisfy the SPR condition $PB_e = C_e^T$. Then, since $(\bar{A}_e, B_e, C_e)$ is SPR, one has that $\bar{A}_e^T P + P\bar{A}_e < 0$, or equivalently,

$$(A_e - B_e C_e k_0)^T P + P(A_e - B_e C_e k_0) < -2\lambda_z P < 0\,,$$

and $PB_e = C_e^T$. Thus, the system $([A_e - B_e C_e k_0], B_e, C_e)$ is also SPR. For a **time varying** $k_p(t) = k_p^{nom} + \delta_{k_p}(t)$, one can write

$$A_e(t) = A_e + A_{e1}\delta_{k_p}(t)\,,$$

where $A_e := A_e(t)|_{k_p = k_p^{nom}}$ and $A_{e1} := \begin{bmatrix} 0 & 0 & 0 & 0 \\ -1 & 0 & 0 & 0 \\ 0 & 0 & 0 & 0 \\ 0 & 0 & 0 & 0 \end{bmatrix}$. Moreover, by adding and subtracting $B_e k_0 \tilde{\sigma} = B_e C_e k_0 \tilde{x}$ in (4.76), one can write

$$\dot{\tilde{x}} = (A_e(t) - B_e C_e k_0)\tilde{x} + B_e[-u_0 + d_{eq3} + k_0\tilde{\sigma}]\,, \tag{4.79}$$

or, equivalently,

$$\dot{\tilde{x}} = (A_e - B_e C_e k_0)\tilde{x} + A_{e1}\delta_{k_p}(t)\tilde{x} + B_e[-u_0 + d_{eq3} + k_0\tilde{\sigma}]\,, \tag{4.80}$$

where

$$A_e - B_e C_e k_0 := \begin{bmatrix} -\frac{1}{\tau_{av}} & 0 & 0 & \frac{k_0}{\tau_{av}} \\ -k_p^{nom} & \frac{(l_0\tau_f - 1)}{\tau_f} & \tau_f l_0 & 0 \\ 0 & \frac{1}{\tau_f} & 0 & 0 \\ \kappa_m & \frac{1}{\tau_f} & a_m & -a_m - \kappa_m k_0 \end{bmatrix}.$$

Now, choosing the Lyapunov function $\tilde{V} := \tilde{x}^T P \tilde{x}$ one can obtain

$$\dot{\tilde{V}} = -\tilde{x}^T Q \tilde{x} + 2\tilde{x}^T P B_e[-u_0 + d_{eq3} + k_0\tilde{\sigma}] + \tilde{x}^T(A_{e1}^T P + P A_{e1})\tilde{x}\delta_{k_p}\,,$$

where

$$-Q := (A_e - B_e C_e k_0)^T P + P(A_e - B_e C_e k_0) < -2\lambda_z P < 0\,,$$

Then, one can verify that

$$\dot{\tilde{V}} \leq -2\lambda_z \tilde{V} + 2\tilde{\sigma}[-u_0 + d_{eq3} + k_0\tilde{\sigma}] + \tilde{x}^T(A_{e1}^T P + P A_{e1})\tilde{x}\delta_{k_p}\,.$$

In addition, noting that

$$|\tilde{x}^T(A_{e1}^T P + P A_{e1})\tilde{x}\delta_{k_p}| \leq 2c_1\|\tilde{x}\|^2|\delta_{k_p}| \leq 2\frac{c_1}{\lambda_m(P)}\tilde{V}|\delta_{k_p}|\,,$$

with $c_1 := \|A_{e1}^T P + P A_{e1}\|/2$, one can further write

$$\dot{\tilde{V}} \leq -\left(2\lambda_z - \frac{2c_1}{\lambda_m(P)}|\delta_{k_p}|\right)\tilde{V} + 2\tilde{\sigma}[-u_0 + d_{eq3} + k_0\tilde{\sigma}]\,.$$

Moreover, since $u_0 = \varrho\mathrm{sgn}(\tilde{\sigma})$ with

$$\varrho = \bar{\varrho} + k_0|\tilde{\sigma}|\,,$$

one has that

$$\dot{\tilde{V}} \leq -\left(2\lambda_z - \frac{2c_1}{\lambda_m(P)}|\delta_{k_p}|\right)\tilde{V} + 2|\tilde{\sigma}|[-\bar{\varrho} + |d_{eq3}|]\,.$$

Now, if $\bar{\varrho}(t) \geq |d_{eq3}(t)| + \delta$, then

$$\dot{\tilde{V}} \leq -\left(2\lambda_z - \frac{2c_1}{\lambda_m(P)}|\delta_{k_p}|\right)\tilde{V} - 2|\tilde{\sigma}|\delta < -2\lambda\tilde{V}\,,$$

for

$$2\lambda_z - \frac{2c_1}{\lambda_m(P)}|\delta_{k_p}| > 2\lambda > 0\,,$$

or,

$$|\delta_{k_p}| < (\lambda_z - \lambda)\lambda_m(P)/c_1\,.$$

By the using the Comparison Lemma with discontinuous right-side, Theorem 8 in [17], one has that

$$|\tilde{\sigma}| \leq |\tilde{x}| \leq \sqrt{\frac{\lambda_M(P)}{\lambda_m(P)}} e^{-\frac{\lambda}{2\lambda_M(P)}t} |\tilde{x}(0)| \,.$$

It should be highlighted that the decay rate of λ is limited to the slowest zero of A_e. So, the quadratic stability margin is limited by the amount of uncertainty in δ_{k_p} and the slowest zero.

■

Remark 9 (A Tuning Procedure for $a_m, \kappa_m, \tau_f, \tau_{av}, l_0$)

For a fixed k_p^{nom}, the following optimization problem can be solved to tune the SSC: min $[\lambda_z + \alpha \|A_{e1}^T P + P A_{e1}\|^{1/2}]$, subject to

$\tau_f l_0 < 1$, $\tau_{av}\kappa_m l_0 < k_p^{nom}$ *and*

$$\tau_{av}\kappa_m l_0(1 - \tau_f l_0) + \tau_f k_p^{nom}(a_m + l_0) < k_p^{nom} \,,$$

where $\alpha > 0$ is a design constant. ■

4.3.2 Modulation Function Implementation

For the modulation function implementation, considering the relative degree two case, only the signals $\ddot{z}_r, e$ and u_{nom} are available. Signals $\dot{e}$ and σ are not available. Moreover, the constant g is known (but just an upper bound is really needed). Thus, recalling that the disturbance D is given by

$$D := u_{nom} + \frac{1}{k_p}[-g - \ddot{z}_r - l_0^2 e] \,.$$

then the following norm bound holds

$$|D| \leq |u_{nom}| + \frac{1}{\underline{k}_p}\omega_1 \,,$$

where $\omega_1 := |-g - \ddot{z}_r - l_0^2 e|$ is an available signal. In addition,

$$|k_p D| \leq \bar{k}_p |u_{nom}| + \omega_1 \,.$$

Since the *equivalent input disturbance* d_{eq3} can be rewritten as

$$d_{eq3} := \eta_1 + \frac{1}{\kappa_m}\eta_2 + \frac{a_m}{\kappa_m}\eta_3 \,, \tag{4.81}$$

a norm observer for the η_1-dynamics, η_2-dynamics and for the η_3-dynamics is needed.

Define the η-dynamics by:

$$\bar{\tau}\dot{\eta} = A_\eta \eta + B_\eta k_p D\,,$$

where $\bar{\tau} := \tau_{av}\tau_f\kappa_m$,

$$A_\eta := \begin{bmatrix} 0 & \tau_f & a_m\tau_f \\ -\kappa_m\tau_{av}k_p & \kappa_m\tau_{av}(l_0\tau_f - 1) & \kappa_m\tau_{av}l_0 \\ 0 & \kappa_m\tau_{av}\tau_f & 0 \end{bmatrix},$$

and $B_\eta := \begin{bmatrix} 0 \\ \kappa_m\tau_{av} \\ 0 \end{bmatrix}$.

4.3.3 Closed-Loop Convergence Analysis

In fact, the following theorem holds.

Theorem 10 *Assume that the velocity $\dot{z}$ is NOT available and (**H1**) and (**H2**) hold. Consider the plant (3.4) with output tracking error (4.1), SSC control law (4.6), (4.7), (4.8) with sliding variable $\tilde{\sigma}$ in (4.4), prediction error (4.5) and modulation function $\varrho = \bar{\varrho} + k_0|\tilde{\sigma}|$, with $\bar{\varrho}$ in (4.39) satisfying (4.77) and k_0 being an appropriate constant. The desired trajectory to be followed is described in (3.6). Then, for sufficiently small time constants of the linear lead filter (τ_f) in (4.3) and the smooth filter (τ_{av}) in (4.7), the tracking error e converges to a small residual set of order $\mathcal{O}(\tau_{av} + \tau_f)$ and the following inequality holds*

$$|e(t)| \leq \mathcal{O}(\tau_{av} + \tau_f) + \pi_e\,, \tag{4.82}$$

where π_e is a vanishing term depending on the initial conditions and this residual set does not depend on the initial conditions. In addition, all closed-loop signals remain uniformly bounded.

Proof: See Appendix A. ∎

4.4 Numerical Simulations

By substituting SSC's u^{nom} with an adaptive law, the SSC can be interpreted as a Robust Adaptive Controller [18]. Indeed, from (3.4), the error tracking dynamics (3.5) can be rewritten as $\ddot{e} = \frac{1}{\Theta^*(t)}u - g - \ddot{z}_r$.

Notice Θ^* varies with time, unlike the usual parameterization found in Model Reference Control literature (MRC). Recalling that $\sigma = \dot{e} + K_1 e$, we can write:

$\dot{\sigma} = \ddot{e} + K_1\dot{e} = \frac{1}{\Theta^*}u - g - \ddot{z}_r + K_1\dot{e}$, or yet,

$$\Theta^*\dot{\sigma} = u - u^*\,, \tag{4.83}$$

where $u^* := \Theta^*\varphi$ and $\varphi := (g + \ddot{z}_r - K_1\dot{e})$. For the case when $\dot{z}$ **is measured**, the signals $\dot{e}$, σ and φ are available. The nominal part of the SSC is defined as: $u^{nom} = \Theta\varphi$, with the parameter Θ given by the gradient law $\dot{\Theta} = -\gamma\sigma\varphi$, with adaptation gain $\gamma > 0$. In this sense, this paper contains a second contribution to the SSC scheme. As in Robust Adaptive Control topology [18], that is, the topology formed by an adaptive part and a robust part, the former also aims to reduce the magnitude of control action (modulation function).

In the following simulations, the Ground Effect gain is considered unknown for the controller design and given by (3.2) with $R = 0.16$m and $\rho = 1.184$. To simulate the payload release we consider the UAV mass varying while constant by parts, in accordance with $m(t) = \frac{1}{0.01s+1}\mu(t)$ and

$$\mu(t) = \begin{cases} 4.0, & \text{para } 0 < t < 30, \\ 3.5, & \text{para } t \geqslant 30\,. \end{cases} \tag{4.84}$$

It's worth noting that, according to [19], one can make $m(t) = \mu(t)$, without altering the closed-loop differential equation solution in the sense of Lebesgue. The plant is described in [19], with $g = 9.81$, $I_x = 0.082$, $I_y = 0.082$ and $I_z = 0.149$.

The UAV's position ($p = [x\ y]^T$), attitude ($q = [\phi\ \theta]^T$) and heading (ψ) are regulated to zero using conventional PD controllers (tuned by trial and error) with the gains: $K_P^q = \left[\begin{smallmatrix}1 & 0\\ 0 & 4\end{smallmatrix}\right]$, $K_D^q = \left[\begin{smallmatrix}1 & 0\\ 0 & 4\end{smallmatrix}\right]$, $K_P^p = \left[\begin{smallmatrix}1 & 0\\ 0 & 4\end{smallmatrix}\right]$, $K_D^p = \left[\begin{smallmatrix}1 & 0\\ 0 & 4\end{smallmatrix}\right]$, $K_P^\psi = 5$ and $K_D^\psi = 2$. The altitude dynamics are given by (3.4), the landing pad oscillates in accordance with (3.1)), with $A = 0.18$ and $\omega = 2\pi/10$, the trajectory to track is described in (3.6) with $\tau_{z_r} = 0.1$, $z_{r_{init}} = 1$ e $z_{r_{bias}} = 0.18$. The SSC controller is implemented with $\tau_{av} = 0.1$, $K_1 = 2$, $a = 5$ and $k = 1$ and the modulation function is implemented as a constant ($\varrho = 50$) for simplicity.

For the adaptive SSC controller $\gamma = 5$. Figure 4.2(a) shows the performance of the SSC without adaptation in closed-loop. Note that both schemes ensure trajectory tracking, but the adaptive SSC shows more transient oscillation. Additionally, the robustness of the SSC regarding the payload release at $t = 30$ is made evident on the control signal in Figure 4.2(b).

It is also noteworthy that both control schemes (with and without adaptation) give similar control signals after $t = 10s$, since the landing pad acceleration $\ddot{z}_d$ in $\ddot{z}_r$ is small. In case of higher accelerations, the adaptive action reduces the disturbance. This can be observed in Figure 4.3(b), where, after the transitory part, the term $\left|-\frac{1}{\Theta^*}u^* + \frac{1}{\Theta^*}u^{nom}\right|$ is practically constant when there is no adaptation (blue line)

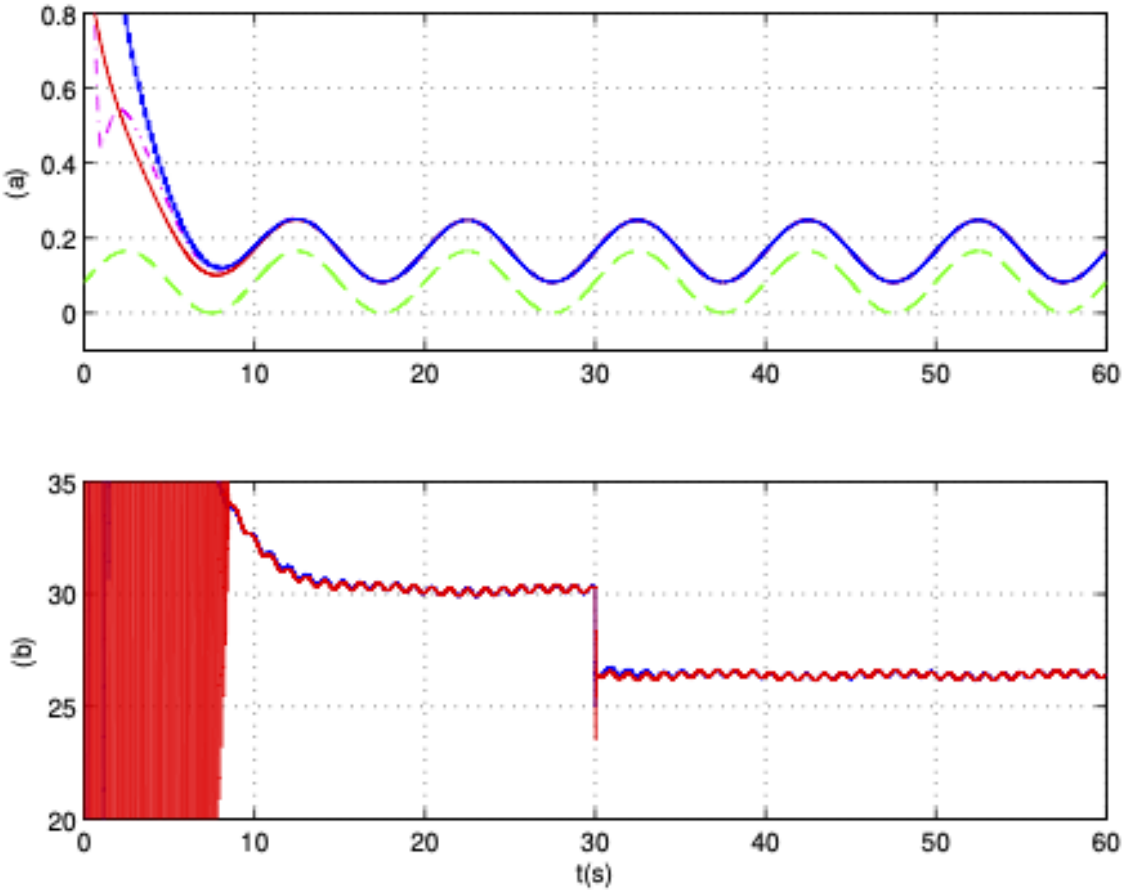

Figure 4.2: Simulation results. Tracking: (a) altitude z_d of landing pad (green), desired trajectory (red), UAV altitude using SSC controller with (magenta) and without (blue) adaptation; (b) control signal using SSC controller with (red) and without (blue) adaptation.

and considerably reduced with adaptation (red line). The reduction happens exactly when Θ approaches Θ^*, see Figure 4.3(b). The adaptive SSC tracks the reference perfectly, with similar results (Figures not shown due to size limitations) to the Adaptive Robust controller [18].

4.5 Experimental Results: Crazyfile UAV and UAV Prototype

For the first experiment a prototype UAV was designed for this work. All hardware details can be found in [19]. In this section, two experiments are highlighted: one for regulation and another for heading tracking. A pilot manually controls x, y and z by means of a joystick with F_z, ϕ_r and θ_r as control signals. The attitude of the UAV is controlled by a PD with gains $K_P^q = 2I$ and $K_D^q = 0.5I$ with I being the identity matrix. The heading is controlled by a PD with gains $K_P^\psi = 1$ and $K_D^\psi = 0.3$ with

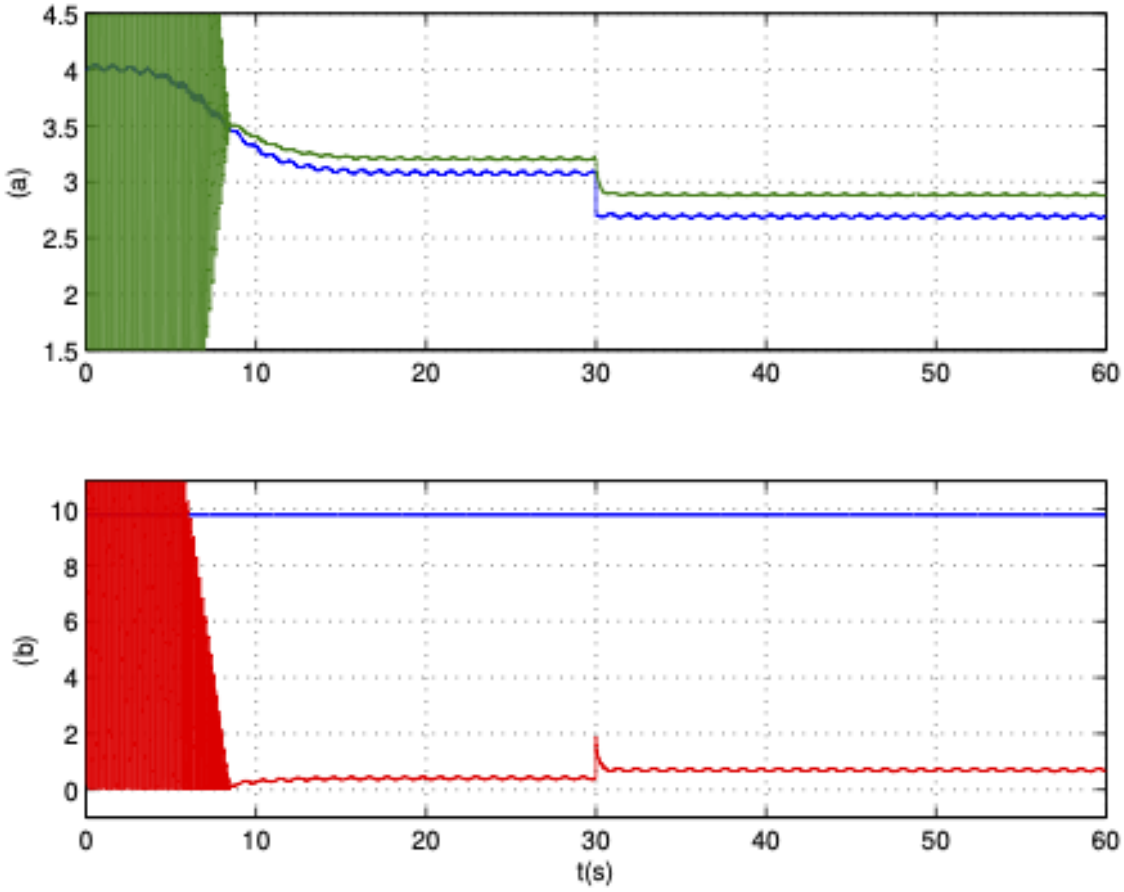

Figure 4.3: Simulation results. Adaptation: (a) time series of ideal signal $\Theta^*(t)$ (blue) and the corresponding adapted signal $\theta(t)$ (green); (b) the term $\left(-\frac{1}{\Theta^*}u^* + \frac{1}{\Theta^*}u^{nom}\right) = \frac{(\Theta-\Theta^*)}{\Theta^*}\varphi$ with (red) and without (blue) adaptation.

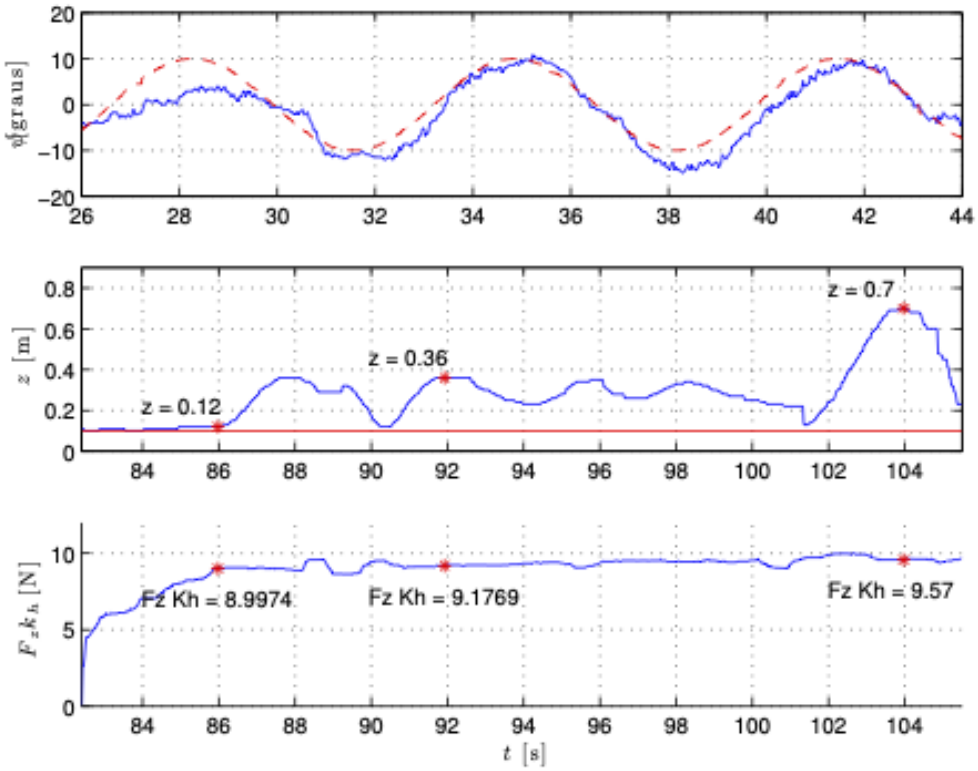

Figure 4.4: Experimental results with manually controlled position (x, y and z) and PD controller for heading: (a) heading (ψ) tracking; (b) regulated heading, altitude z (blue) and ground level (red); (c) time series for $k_h u = F_z k_h$.

a sinusoidal reference signal $\psi_r = 10\sin(2\pi 0.15t)$.

Figure 4.4(a) shows the proper tracking of the heading ψ with sinusoidal reference signal, albeit the presence of disturbances from the change in attitude and altitude.

On another flight, the heading was regulated to zero to observe the presence of Ground Effect. Figure 4.4(b) shows the altitude z (in blue) and the ground (red line), with an offset due to ultrasonic sensor position. Figure 4.4(c) presents the control signal F_z through the product $F_z k_h$ as defined in (3.4), making the presence of Ground Effect evident. This product corresponds to a more accurate approximation of the vertical force acting on the UAV since it takes the attitude into account.

The red asterisks in z and F_z in Figure 4.4 indicate instants where the vertical velocity was nearly zero. There is no mass variation during this experiment.

In order to show the robustness capability of the proposed control scheme second experiment with a considerable smaller UAV was considered. We use the Crazyflie 2.0 which is an open-source nano UAV designed by Bitcraze, in Sweden. The presence of Ground Effect is also evident, as illustrated by the Figure 4.5(c), where the average control signal reduces after $t = 30$s, as the UAV approaches the ground level. Figure 4.6 illustrates the tracking of the desired reference z_r before approaching the

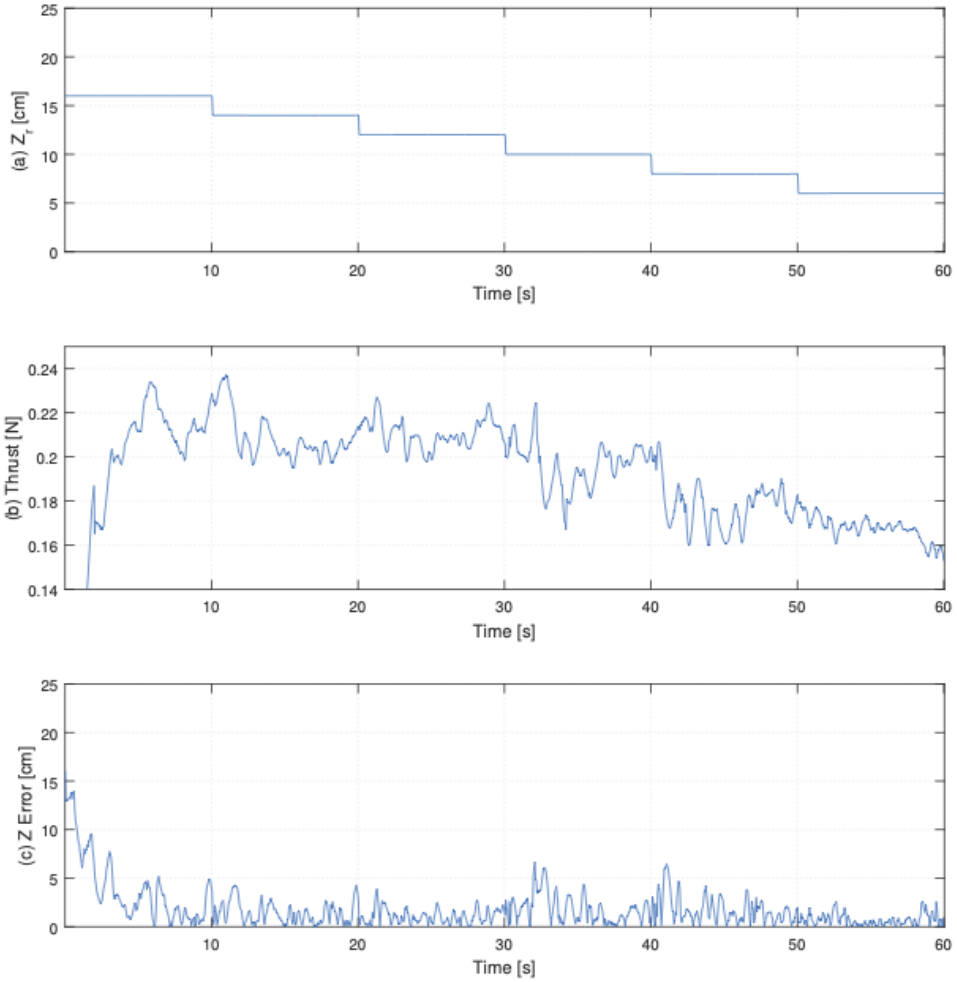

Figure 4.5: Experimental results with the Crazyflie UAV to illustrate the Ground Effect. PD controller regulating position (x, y and z) and attitude: (a) the desired altitude; (b) the control effort; (c) the tracking error. All vertical positions in cm.

landing pad. Then, in sequel, in Figure 4.7 one can observe the UAV approaching the moving landing pad.

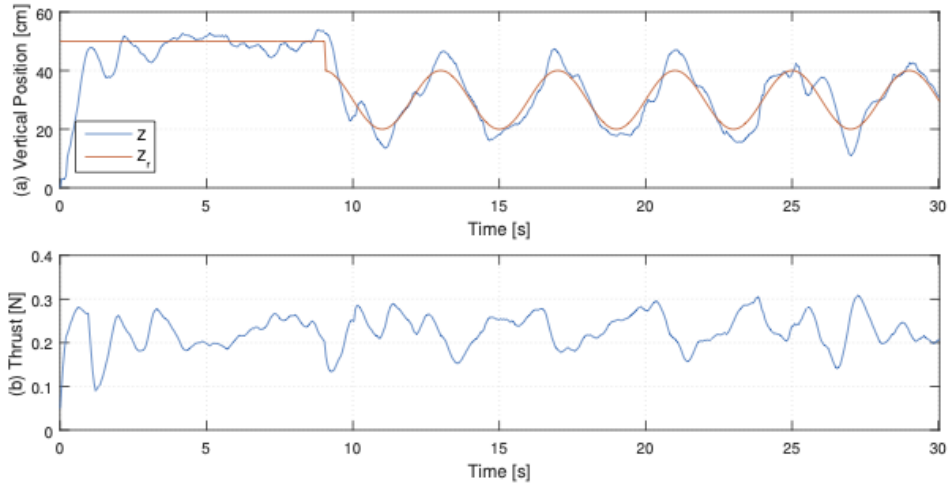

Figure 4.6: Experimental results with the Crazyflie UAV to illustrate the tracking performance. PD controller regulating position (x, y and z) and attitude: (a) the desired altitude z_r (red) and the actual UAV altitude z (blue); (b) the control effort. All vertical positions in cm.

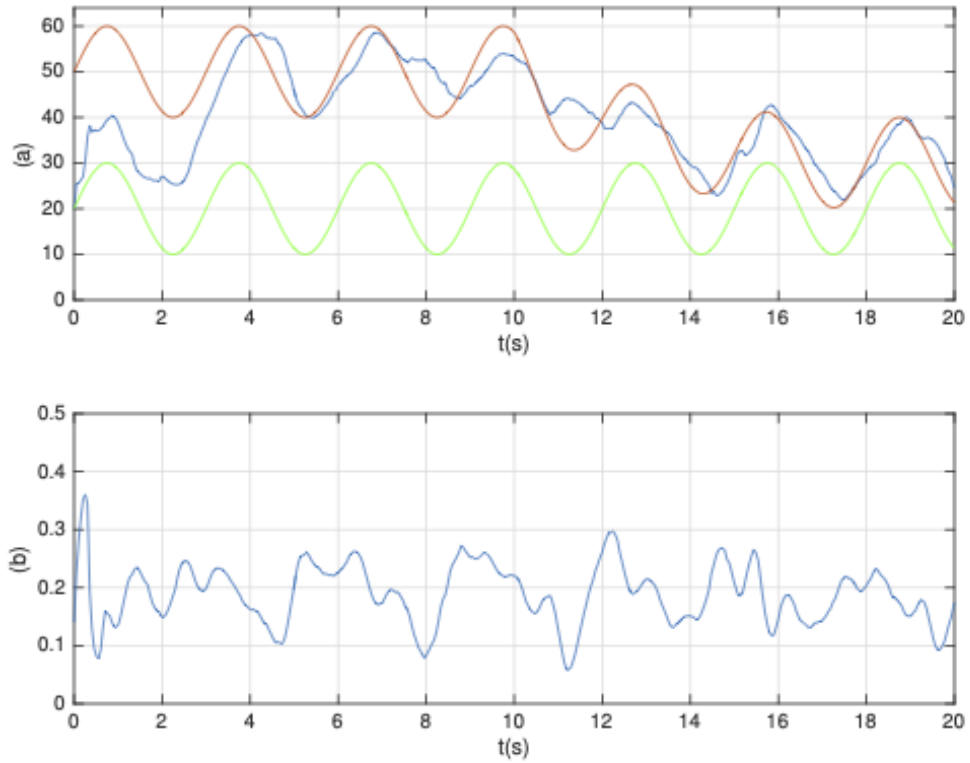

Figure 4.7: Experimental results with the Crazyflie UAV to illustrate a landing on an oscillatory platform. PD controller regulating position (x, y and z) and attitude: (a) the desired altitude z_r (red), the landing pad displacement z_d (green) and the actual UAV altitude z (blue); (b) the control effort. All vertical positions in cm.

Chapter 5

Implementation for Simulations and Experiments

In order to run experiments and test the theory, methods were implemented and systems were built to assist the entire process. For an insightful and repeatable experimental campaign, the following qualities must be pursued:

- Weather independence.
- Failure acceptance while isolated from financial consequence.

  If financial consequence is unavoidable, at least it must not impact the schedule significantly.
- Real world correlation.

A complete simulation environment provides the security needed to employ a bold experimental strategy, while state-of-the-art laboratory hardware provides a reliable connection with reality.

5.1 Simulation

5.1.1 Multi-rotor Dynamic Simulation

Gazebo is a dynamic multi-body simulation environment widely used for robotic development, see Figure 5.1. It allows the creation of case-oriented "worlds", models, sensors, actuators, etc. With sufficiently powerful hardware, real-time simulations are possible. Arguably the main reason for its popularity is the integration with ROS, which allows the same computer used to control the real robot to be used in a simulated robot seamlessly, although it is also a conveniently simple physics engine on its own. In the case of a multi-rotor, one can assemble an arm model that will

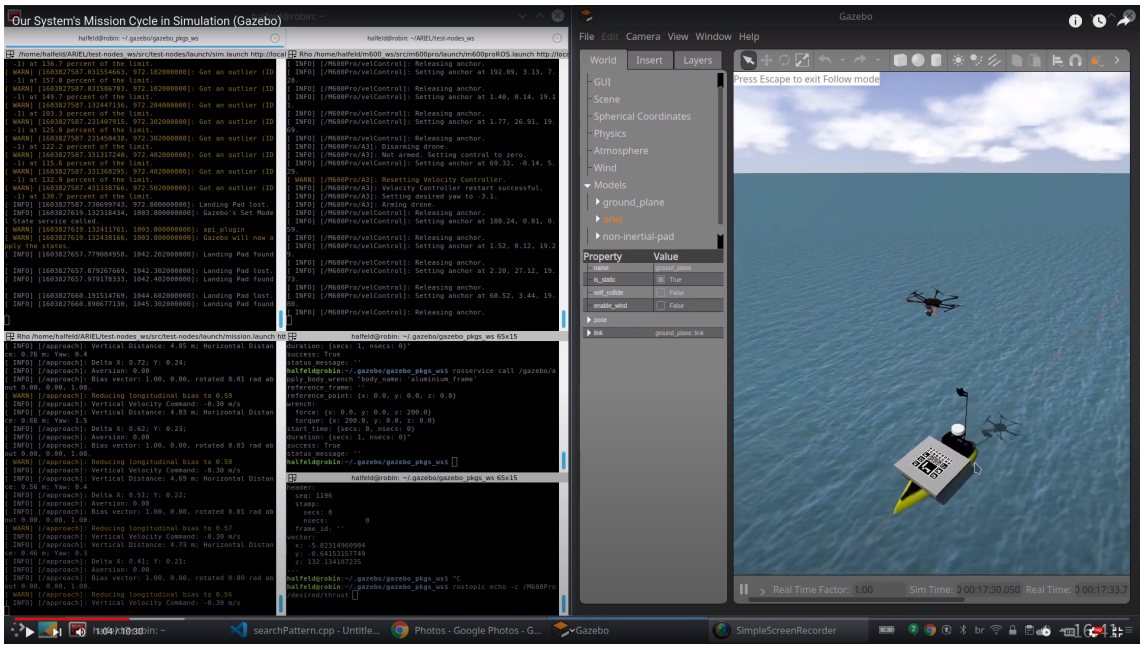

Figure 5.1: Gazebo simulation of a Multi-rotor landing on a moving boat. On the left, several terminals running ROS nodes.

be reused for each arm of the multi-rotor. Since most multi-rotor configurations use clockwise and counter-clockwise propellers, two separate models are required. If there are graphical differences, such as a different color mount, the number of models doubles. In the case of the M600, 4 models were coded - two with mirrored propeller and two with color change. In fact, the M600 model could have been a written as a single model, but including separate models of the arm makes them a useful model for other multi-rotors and other non-orthodox robots, specially since the arm for the M600 Pro is commercially available as a product named DJI E2000 Pro.

These models can all made available online. [1]

Models can be extended through plug-ins. External programs can interface with Gazebo this way. One such plugin allows external ROS nodes to apply forces and moments on any given part of the model structure. It has been used to act on the motors.

The framework also allows the creation of sensors. GPS, IMU, cameras, etc. are readily available for configuration and use. Even noise can be introduced as an option.

If properly setup with namespaces, several entities of the robot can be used in the simulation and controlled independently, just as if there were different instances of the actual robot. Aside from the significant reduction in budget requirement for multi-agent experiments, doing so in a simulated environment protects the involved

[1] Please contact ricardo@andrade.com to request access.

personnel and third parties from the much higher risk of aerial accidents.

Additionally, a ROS node was implemented to emulate the behavior of the A3 Pro controller and its ROS wrapper. This provides an compatibility layer ensuring a transparent transition between the simulated model and the real multi-rotor. Some of the implemented capabilities are:

- Control using the generic setpoint topic.

  Velocity, attitude, thrust, etc. control modes.

  FLU and ENU reference frames.

- Arm and disarm services.
- Ground truth topics.
- Sensor topics.

5.1.2 Computational Fluid Dynamics

Unfortunately there is very little cross-talk between different engineering fields and often some of them are limited by problems which are already solved in others. Computational Fluid Dynamics is one of the techniques that rarely permeates robotics. Through the use of several specialized solvers, one can obtain velocity and pressure fields around the multi-rotor, over which aerodynamic forces can be calculated. This technique enables the extraction of propeller characteristics under conditions which are not trivial to experimentally obtain. This information can then feeds a momentum-based approach for the simulation of the entire vehicle under various relative winds. The result is a complete picture of the aerodynamic forces under all relevant attitudes and velocities, which in turn is used to generate an aerodynamic mapping to be used in the estimation of wind.

The limitation of the method lies in the computational power required to run accurate simulations. Domain size, mesh resolution , time-step, etc. can be optimized to some extent, but there is a minimum required for the simulation to make sense. There is also the need to understand the different ways pressure and velocity fields generate aerodynamic forces. It is up to the operator to find the optimum resources and avoid incoherent results. The angular velocity of the propellers and the level of turbulence generated by the multi-rotor are formidable challenges for this task.

5.2 Experimental Setup

The laboratory named LEAD at the Federal University of Rio de Janeiro is privileged to be situated directly in front of the COPPE's Sport Guild's (Grêmio) soccer field,

having access to an open area to perform low altitude aerial experiments virtually any time the weather allows.

A landing pad with several visual markers of type ArUco in different sizes is available. This enables the visual localization of either a static or moving target for multi-rotor operations. Aside from occasional issues with sun reflection at just the wrong angle, it has proved to be a very useful tool for landing experiments. When static, it can also be used as an input for Kalman Filter correction step.

Another key component of the experimental campaign is the dedicated computer network built for it, see Figure 5.2. Equipment from the brand Ubiquiti was selected to provide a reliable and adaptable setup such that the network does not bottleneck the tests. Even so, care must be taken not to use network resources unnecessarily. Streaming video during tests may introduce delays in some of the other messages, and recording ROS Bags locally, i.e, at the Onboard Computer, performs much better as well.

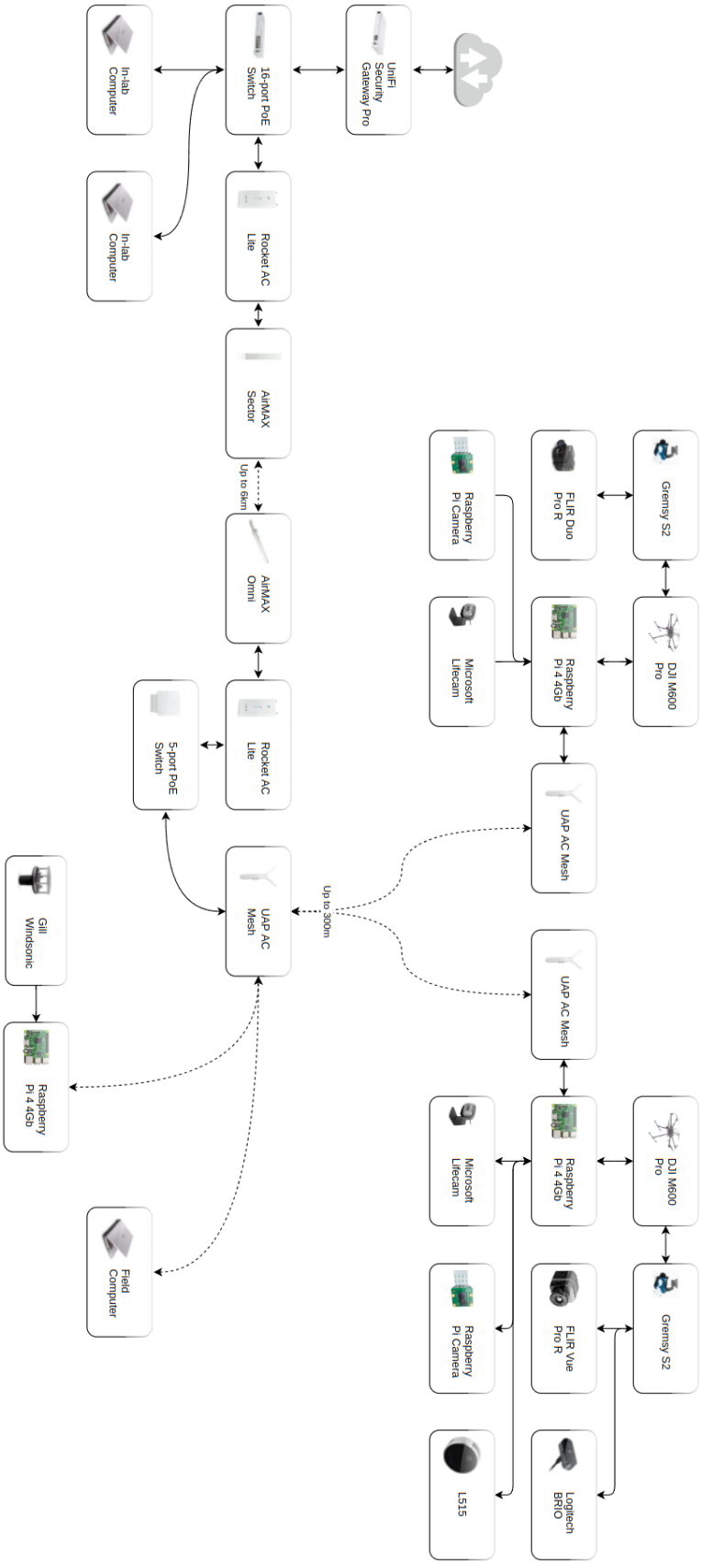

Figure 5.2: The entire network of systems available.

Chapter 6

Conclusion

In this Dissertation, the context of multi-rotor application was introduced and the challenges highlighted. Justification for the emphasis on landing was provided in light of the envisioned near future use-cases.

The presentation of a general mathematical model using quaternion was formalized to consolidate its use in bolder and more aggressive maneuvers required to extend the envelope of multi-rotor applications. A simplified model for vertical approach in landing scenarios was also introduced and used to indicate the compatibility of such a maneuver with the trajectory tracking controller SSC.

In this sense, this work provided a perspective for the problem of landing an UAV in a vertically oscillatory pad under the aerodynamic influence of Ground Effect. It also provides considerations for disturbances arising from payload pick-up/release. For the landing maneuver, a landing pad approximation trajectory is employed for the tracking controller. Aiming to generate a smooth and robust control law, a Smooth Sliding Control (SSC), previously designed for linear plants, was considered and the first generalization of the SSC for this class of nonlinear plants was obtained. One can observe that the adaptive part introduced in the SSC scheme promotes a reduction in the robust control action. Generally speaking, robustness with respect to mass variation and Ground Effect in closed-loop trajectory tracking can be observed. Numerical simulations show the performance of the SSC and experiments with two different UAV illustrate the presence of Ground Effect.

An open-source simulation environment model and control system based on the available DJI Matrice 600 Pro was implemented to reduce operational risk due to untested algorithms prior to testing in the real multi-rotor. The control architecture was thoroughly discussed and the entire operational cycle tested with it before experimenting on the field. An additional node was implemented to make the simulator compatible with higher-level control systems designed for the real multi-rotor and vice-versa. Improvements for modelling were suggested, such as including the advance effect on propeller thrust and torque, usage of the dissociated thrust and

torque polynomial exponents as well as allowing for real numbers.

Clearly there is a very healthy environment for subsequent research and development of multi-rotor related techniques, strategies, operational concepts, controllers and more. In the following bullet points, follow-up research and development topics are:

- Design and implement a trajectory generator and tracker specifically for ideal contact with the pad.
- Perform the closed-Loop convergence analysis and the proof of existence of ideal sliding mode for the extra case.
- Perform a rigours modelling and stability analysis for the control landing scheme based on the 3 control components: rational, canonical and aversive.
- Improve simulator control system to behave more like the actual Matrice 600 Pro.

  Implement advance effect for propeller thrust and torque.

  Implement an aerodynamic node.

  Implement a dissociated real exponent allocation system.

Bibliography

[1] GUENARD, N., HAMEL, T., MOREAU, V. "Dynamic modeling and intuitive control strategy for an "X4-flyer"". In: *2005 International Conference on Control and Automation*, v. 1, pp. 141–146 Vol. 1, June 2005. doi: 10.1109/ICCA.2005.1528106.

[2] BURRI, M., OLEYNIKOVA, H., , et al. "Real-Time Visual-Inertial Mapping, Re-localization and Planning Onboard MAVs in Unknown Environments". In: *Intelligent Robots and Systems (IROS 2015), 2015 IEEE/RSJ International Conference on*, Sept 2015.

[3] FRESK, E., NIKOLAKOPOULOS, G. "Full quaternion based attitude control for a quadrotor". In: *2013 European Control Conference (ECC)*, pp. 3864–3869, July 2013. doi: 10.23919/ECC.2013.6669617.

[4] LEFEBER, E., VAN DEN EIJNDEN, S. J. A. M., NIJMEIJER, H. "Almost global tracking control of a quadrotor UAV on SE(3)". In: *2017 IEEE 56th Annual Conference on Decision and Control (CDC)*, pp. 1175–1180, Dec 2017. doi: 10.1109/CDC.2017.8263815.

[5] OH, S.-R., PATHAK, K., AGRAWAL, S. K., et al. "Approaches for a tether-guided landing of an autonomous helicopter", *IEEE Transactions on Robotics*, v. 22, n. 3, pp. 536–544, June 2006. ISSN: 1552-3098. doi: 10.1109/TRO.2006.870657.

[6] LEE, D., RYAN, T., KIM, H. J. "Autonomous landing of a VTOL UAV on a moving platform using image-based visual servoing". In: *2012 IEEE International Conference on Robotics and Automation*, pp. 971–976, May 2012. doi: 10.1109/ICRA.2012.6224828.

[7] LING, K., CHOW, D., DAS, A., et al. "Autonomous Maritime Landings for Low-Cost VTOL Aerial Vehicles". In: *2014 Canadian Conference on Computer and Robot Vision*, pp. 32–39, May 2014. doi: 10.1109/CRV.2014.13.

[8] DANJUN, L., YAN, Z., ZONGYING, S., et al. "Autonomous landing of quadrotor based on ground effect modelling". In: *2015 34th Chinese Control*

Conference (CCC), pp. 5647–5652, July 2015. doi: 10.1109/ChiCC.2015.7260521.

[9] HSU, L. "Smooth sliding control of uncertain systems based on a prediction error", *Int. J. on Robust and Nonlinear Control*, v. 7, pp. 353–372, 1997.

[10] HSU, L., COSTA, R. R. "Variable structure model reference adaptive control using only input and output measurement: Part I", *Int. J. Contr.*, v. 49, n. 2, pp. 399–416, 1989.

[11] MELLINGER, D., KUMAR, V. "Minimum snap trajectory generation and control for quadrotors". In: *Robotics and Automation (ICRA), 2011 IEEE International Conference on*, pp. 2520–2525. IEEE, 2011.

[12] MUELLER, M. W., HEHN, M., D'ANDREA, R. "A computationally efficient motion primitive for quadrocopter trajectory generation", *IEEE Transactions on Robotics*, v. 31, n. 6, pp. 1294–1310, 2015.

[13] LANDRY, B., DEITS, R., FLORENCE, P. R., et al. "Aggressive quadrotor flight through cluttered environments using mixed integer programming". In: *2016 IEEE International Conference on Robotics and Automation (ICRA)*, pp. 1469–1475, May 2016. doi: 10.1109/ICRA.2016.7487282.

[14] KHALIL, H. K. *Nonlinear Systems*. 3^{rd} ed. , Prentice Hall, 2002.

[15] HSU, L., LIZARRALDE, F., ARAÚJO, A. "New results on output-feedback variable structure adaptive control: design and stability analysis", *IEEE Trans. Aut. Contr.*, v. 42, n. 3, pp. 386–393, 1997.

[16] IOANNOU, P., SUN, J. *Robust Adaptive Control*. Prentice-Hall, 1996.

[17] FILIPPOV, A. F. "Differential equations with discontinuous right-hand side", *American Math. Soc. Translations*, v. 42, n. 2, pp. 199–231, 1964.

[18] HU, B., LU, L., MISHRA, S. "Fast, safe and precise landing of a quadrotor on an oscillating platform", *American Control Conference - Chicago, IL, USA*, pp. 3836–3841, 2015.

[19] CATUNDA, P. R. Y. *Controle Robusto Suave Aplicado ao Pouso de Quadrirrotores*. Dissertação, Programa de Engenharia Elétrica - Universiade Federal do Rio de Janeiro, Rio de Janeiro, Março 2016.

[20] HSU, L. "Smooth Sliding Control of Uncertain Systems Based on a Prediction Error", *International Journal of Robust and Nonlinear Control*, v. 7, n. 4, pp. 353–372, 1997. ISSN: 1099-1239.

[21] PEIXOTO, A., LIZARRALDE, F., HSU, L. "Further Results on Smooth Sliding Control of Uncertain Systems". In: *Proc. American Contr. Conf.*, pp. 2380–2385, Anchorage, 2002.

[22] PEIXOTO, A., LIZARRALDE, F., HSU, L. "Experimental Results on Smooth Sliding Control of Uncertain Systems". In: *Proceedings of the 2001 IEEE International Conference on Decision and Control*, pp. 928 – 933, Orlando, Florida USA, 2001.

[23] OLIVEIRA, T. R., HSU, L., NUNES, E. V. L. "Smooth sliding control to overcome chattering arising in classical SMC and super-twisting algorithm in the presence of unmodeled dynamics", *Journal of the Franklin Institute*, v. 359, n. 2, pp. 1235–1256, 2022.

[24] PEIXOTO, A., LIZARRALDE, F., HSU, L. "Further Results on Smooth Sliding Control of Uncertain Systems". In: *Proceedings of the 2002 American Control Conference*, pp. 2380–2385, Anchorage (Alaska), 2002.

[25] PEIXOTO, A., LIZARRALDE, F., HSU, L. "Experimental Results on Smooth Sliding Control of Uncertain Systems". In: *Proceedings of the 2001 IEEE International Conference on Decision and Control*, pp. 928 – 933, Orlando, Florida USA, 2001.

[26] UTKIN, V. I. *Sliding Modes in Control and Optimization.* Springer-Verlag, 1992.

[27] HSU, L. "Variable structure model-reference adaptive control (VS-MRAC) using only input and output measurements. II". In: *Decision and Control, 1988., Proceedings of the 27th IEEE Conference on*, pp. 2396–2401 vol.3, Dec 1988. doi: 10.1109/CDC.1988.194770.

Appendix A

Main Proofs

A.1 Proof of Lemma 1

From (4.7), one has that $u_0 - u_0^{av} = \tau_{av}\dot{u}_0^{av}$, then the prediction error dynamics can be rewritten as $\dot{\bar{\sigma}} = -a_m\bar{\sigma} + \kappa_m\tau_{av}\dot{u}_0^{av}$. By defining the auxiliary signal $\sigma_a := -\kappa_m\tau_{av}u_0^{av} + \bar{\sigma}$, one also has that $\dot{\sigma}_a = -a_m\sigma_a + a_m\kappa_m\tau_{av}u_0^{av}$. Consequently, the σ_a-dynamics is ISS w.r.t. u_{av}, with a small gain $\kappa_m\tau_{av}$, and (4.9) holds. ∎

A.2 Proof of Lemma 12

From (4.5), one has that $[u_0 - u_0^{av}] = [\dot{\bar{\sigma}} + a_m\bar{\sigma}]/\kappa_m$ and, consequently, one can further write

$$\dot{\epsilon} + a_m\epsilon = k_p[-u_0 + U_d] - \frac{(\kappa_m - k_p)}{\kappa_m}[\dot{\bar{\sigma}} + a_m\bar{\sigma}]\,. \tag{A.1}$$

Now, considering the auxiliary variable $\sigma_b := \epsilon + \frac{(\kappa_m - k_p)}{\kappa_m}\bar{\sigma}$ one has

$$\dot{\sigma}_b + a_m\sigma_b = k_p[-u_0 + U_d] - \frac{\dot{k}_p}{\kappa_m}\bar{\sigma}\,. \tag{A.2}$$

Hence, the time derivative of $V := \sigma_b^2/2$ along the solutions of (A.2) is given by:

$$\dot{V} + 2a_mV = -k_p\sigma_bu_0 + k_p\sigma_bU_d - \sigma_b\left[\frac{\dot{k}_p}{\kappa_m}\right]\bar{\sigma}\,.$$

For $|\epsilon| > \left|\frac{(\kappa_m - k_p)}{\kappa_m}\right||\bar{\sigma}|$ is clear that $\mathrm{sgn}(\epsilon) = \mathrm{sgn}(\sigma_b)$ so that $u_0 = \varrho(t)\mathrm{sgn}(\epsilon) = \varrho(t)\mathrm{sgn}(\sigma_b)$. Therefore, $\dot{V}$ satisfies

$$\dot{V} + 2a_mV = -k_p\varrho|\sigma_b| + k_p\sigma_bU_d - \sigma_b\left[\frac{\dot{k}_p}{\kappa_m}\right]\bar{\sigma}\,.$$

and

$$\dot{V} \leq -2a_m V + k_p|\sigma_b| \left\{ -\varrho + |U_d| + \left| \frac{\dot{k}_p}{k_p \kappa_m} \right| |\bar{\sigma}| \right\} .$$

Finally, if the modulation function ϱ is designed so that

$$\varrho \geq |U_d| + \left| \frac{\dot{k}_p}{k_p \kappa_m} \right| |\bar{\sigma}| + \delta \,,$$

where $\delta > 0$ is an arbitrary positive constant, it is assured that $\dot{V} < -2a_m V$ and $V, \sigma_a < \Pi$, where Π is a vanishing term. Hence,

$$|\epsilon| - \left| \frac{(\kappa_m - k_p)}{\kappa_m} \bar{\sigma} \right| \leq |\sigma_b| < \Pi \,,$$

and

$$|\epsilon| \leq \left| \frac{(\kappa_m - k_p)}{\kappa_m} \bar{\sigma} \right| + \Pi \,,$$

from which one can conclude that the ϵ-dynamics is ISS w.r.t. $\tau_{av}|u_0^{av}|$ by using Lemma 1 and the upper bound for $k_p(t)$ obtained from **(H1.c)** and **(H2.b)**. ∎

A.3 Proof of Lemma 8

Let

$$\tilde{x} := \begin{bmatrix} \epsilon & \sigma_c \end{bmatrix}^T . \tag{A.3}$$

Thus, one can write:

$$\dot{\tilde{x}} = A_e(t)\tilde{x} + B_e[u_0 + d_{eq}] \,, \quad \epsilon = C_e \tilde{x}, \tag{A.4}$$

where $A_e(t) := \begin{bmatrix} -a_m & \kappa_m - k_p(t) \\ 0 & -1/\tau_{av} \end{bmatrix}$, $B_e := \begin{bmatrix} -\kappa_m & 1/\tau_{av} \end{bmatrix}^T$ and $C_e := \begin{bmatrix} 1 & 0 \end{bmatrix}$.
By adding and subtracting $B_e k_0 \epsilon = B_e C_e k_0 \tilde{x}$, one can write

$$\dot{\tilde{x}} = \bar{A}_e(t)\tilde{x} + B_e[u_0 + d_{eq} - k_0\epsilon] \,, \quad \epsilon = C_e \tilde{x}, \tag{A.5}$$

where

$$\bar{A}_e(t) := A_e(t) + B_e C_e k_0 = \begin{bmatrix} -a_m - k_0\kappa_m & \kappa_m - k_p(t) \\ k_0/\tau_{av} & -1/\tau_{av} \end{bmatrix} .$$

When $k_p(t)$ is a constant, the system (A_e, B_e, C_e) is Almost Strictly Positive Real (ASPR). Indeed, since $C_e B_e = -\kappa_m \neq 0$, then (A_e, B_e, C_e) has relative degree one. Moreover, by using the Rosenbrock system matrix, the triple (A_e, B_e, C_e) is minimum phase. The existence of a large enough k_0 such that $(\bar{A}_e, B_e, C_e)$ is SPR

is assured.

For a time varying $k_p(t)$, a similar conclusion can be obtained by choosing the Lyapunov function $\tilde{V} := \tilde{x}^T P \tilde{x}$ with $P = P^T = \begin{bmatrix} \frac{\tau_{av}+1}{\tau_{av}\kappa_m} & 1 \\ 1 & \tau_{av}\kappa_m \end{bmatrix} > 0$. In fact, one can verify that $\bar{A}_e^T(t)P + P\bar{A}_e(t) < 0$ $(\forall t)$, for a sufficiently large k_0. Then, the proof follows the steps in [27]. ∎

A.4 Proof of Theorem 5

From Lemmas 1 and 12, the prediction error dynamics and the sliding variable dynamics are ISS w.r.t. u_0^{av} with ISS gain of order $\mathcal{O}(\tau_{av})$. In addition, since $\sigma = \epsilon + \bar{\sigma}$, the σ-dynamics and the e-dynamics $\sigma = \dot{e} + e$ are also ISS w.r.t. u_0^{av} with ISS gain of order $\mathcal{O}(\tau_{av})$.

Note that the modulation function ϱ designed to satisfy both inequalities appearing in Lemma 8 and Lemma 12 requires norm bounds for the signals $U_d, \bar{\sigma}$, σ_d, k_p and $\dot{k}_p$. Hence, the modulation function can be designed to satisfy both inequalities appearing in Lemma 8 and Lemma 12 and, in addition, the following inequality

$$|\varrho(t)| \leq k_{\varrho 1}\tau_{av}|u_0^{av}(t)| + k_{\varrho 2} + \pi_\varrho \,, \tag{A.6}$$

where $\pi_\varrho := \beta_\varrho(|\epsilon(0)| + |\bar{\sigma}(0)| + |\sigma_d(0)|)e^{-\lambda_\varrho t}$, $\beta_\varrho \in \mathcal{K}_\infty$, $0 < \lambda_\varrho < a_m$ and $k_{\varrho 1}, k_{\varrho 2} > 0$ are appropriate constants. Therefore, by considering the smooth filter dynamics $\tau_{av}\dot{u}_0^{av} + u_0^{av} = u_0 = \varrho \mathrm{sgn}(\epsilon)$, one can conclude that u_0^{av} is uniformly norm bounded and, consequently, all Closed-Loop signal are also uniformly norm bounded and the tracking error converges to a residual set of order $\mathcal{O}(\tau_{av})$. ∎

A.5 Proof of Theorem 10

The proof is carried out by following similar steps of the relative degree one case. The proof is omitted to save space. ∎

A.6 Extra Lemmas

A.6.1 Auxiliary Lemma 11

The following auxiliary lemma can be stated.

Lemma 11 *Consider a first order strictly stable dynamics*

$$\tau\dot{x}(t) \;=\; -\lambda x(t) + u(x,t)\,, \quad x(0) = x_0\,, \tag{A.7}$$

defined almost everywhere, *where* $\tau, \lambda > 0$ *and* u *is* L.I. *input function which is allowed to be discontinuous, satisfying*

$$|u| \leq U(t)\,,$$

for some well defined (smooth) function $U(t)$*. The solutions of (A.7) are absolutely continuous (by definition) and are understood in the sense of Filippov [17] when, eventually, sliding mode takes place at* $x \equiv 0$*. Let* $[0, t_M)$ *the maximum interval for the definition of solutions. Then, the first order system*

$$\tau\dot{\omega}(t) = -\lambda\omega(t) + U(t)\,, \quad \omega(0) = |x(0)|\,,$$

is a norm observer for the x*-dynamics (A.7) and one can write*

$$|x(t)| \leq \omega(t)\,, \quad \forall t \geq 0\,,$$

almost everywhere. *Moreover, the* ω*-dynamics is ISS w.r.t.* U *with ISS gain* independent *of* τ*.*

Proof:

Proof when $u(t)$ is well defined:

The solution of the x-dynamics (A.7) is given by

$$x(t) = \frac{1}{\tau}\int_0^t e^{-\frac{\lambda}{\tau}(t-\nu)}u(x(\nu),\nu)d\nu + e^{-\frac{\lambda}{\tau}t}x(0)\,, \quad \forall t \geq 0\,,$$

when $u(x(t), t)$ is well defined, $\forall t \geq 0$. Thus, subsequently, one can write

$$|x(t)| \leq \frac{1}{\tau}\left|\int_0^t e^{-\frac{\lambda}{\tau}(t-\nu)}u(x(\nu),\nu)d\nu\right| + e^{-\frac{\lambda}{\tau}t}|x(0)|\,, \quad \forall t \geq 0\,,$$

$$|x| \leq \frac{1}{\tau}\int_0^t e^{-\frac{\lambda}{\tau}(t-\nu)}|u(x(\nu),\nu)|d\nu + e^{-\frac{\lambda}{\tau}t}|x(0)|\,, \quad \forall t \geq 0\,,$$

and

$$|x| \leq \frac{1}{\tau}\int_0^t e^{-\frac{\lambda}{\tau}(t-\nu)}|U(\nu)|d\nu + e^{-\frac{\lambda}{\tau}t}|x(0)| := \omega\,, \quad \forall t \geq 0\,,$$

where the relationship $|u| \leq U$ was used to obtain the last inequality and ω is the solution of the first order system

$$\tau\dot{\omega} = -\lambda\omega + U\,, \quad \omega(0) = |x(0)|\,.$$

■

Proof for u discontinuous - with "division by zero" $(1/|x|)$:

First, consider the time sequence $0 < t_1 < t_2 < \ldots$, where $|x(t)|$ cross zero or reaches/leave sliding mode at the surface $x(t) = 0$. Note that $x(t_1) = x(t_2) = \ldots = 0$. The x-dynamics (A.7) given by

$$\tau\dot{x} \;\; = \;\; -\lambda x + u\,, \tag{A.8}$$

is defined *almost everywhere*, with any solution $x(t)$ in the sense of Filippov being *absolutely continuous*. Thus, one can obtain the solution $x(t)$ for $t \in (t_k, t_{k+1})$ and for $k = 1, 2, \ldots$, by taking the time instant t_k as the initial time with zero initial condition $(x(t_k) = 0)$.

Letting $V := x^2$, from (A.8), one has that

$$\tau\dot{V} = 2x\tau\dot{x} = -2\lambda V + 2xu\,,$$

holds *almost everywhere*. Moreover, defining $W^2 := V$ one can also write that $2\dot{W}W = \dot{V}$ and $\tau W\dot{W} = -\lambda W^2 + xu$. Since $W = |x|$, one also has that the inequality

$$\tau W\dot{W} \leq -\lambda W^2 + WU\,,$$

holds *almost everywhere*. In addition, taking any time interval (t_k, t_{k+1}) where $x(t)$ is not in sliding motion $\forall t \in (t_k, t_{k+1})$, one has $W(t) \neq 0$ and, consequently:

$$\tau\dot{W}(t) \leq -\lambda W(t) + U(t)\,, \quad t \in (t_k, t_{k+1})\,, \quad W(t_k) = 0\,.$$

Thus, by using the Comparison Lemma with discontinuous right-hand side, Theorem 8 in [17], one has that

$$W(t) \leq \omega(t)\,, \quad t \in [t_k, t_{k+1}]\,,$$

almost everywhere, where $\omega(t)$ is the solution of

$$\tau\dot{\omega}(t) = -\lambda\omega(t) + U(t)\,, \quad \omega(t_k) = 0\,.$$

One can further write that:

$$W(t) \leq \omega(t) = \frac{1}{\tau}\int_{t_k}^{t} e^{-\frac{\lambda}{\tau}(t-\nu)}U(\nu)d\nu \leq \frac{1}{\tau}\int_{0}^{t} e^{-\frac{\lambda}{\tau}(t-\nu)}U(\nu)d\nu\,,$$

$\forall t \in [t_k, t_{k+1}]$, since $U(t) \geq 0$, $\forall t$. Hence, since this norm bound holds for all t_k such that $x(t)$ is not in sliding motion $\forall t \in (t_k, t_{k+1})$ one has it holds $\forall t \in [t_1, t_M]$, including the interval where $x(t) = 0$ $(W(t) = |x(t)| = 0)$ is in sliding motion.

Hence, one can write

$$W(t) \leq \frac{1}{\tau}\int_0^t e^{-\frac{\lambda}{\tau}(t-\nu)}U(\nu)d\nu\,, \quad \forall t \in [t_1, t_M]\,. \tag{A.9}$$

Now, lets verify the interval $[0, t_1)$. First, note that if $x(0) = 0$ then $t_1 = 0$. Otherwise, one has that $W(t) \neq 0$, $\forall t \in [0, t_1)$, and thus

$$\tau\dot{W}(t) \leq -\lambda W(t) + U(t)\,, \quad t \in (0, t_1)\,,$$

and $W(0) = |x_0| > 0$. Thus, by using again the Comparison Lemma with discontinuous right-hand side, Theorem 8 in [17], one has that

$$W(t) \leq \omega(t)\,, \quad t \in [0, t_1]\,,$$

almost everywhere in $[0, t_1]$, where $\omega(t)$ is now the solution of

$$\tau\dot{\omega}(t) = -\lambda\omega(t) + U(t)\,, \quad \omega(0) = |x_0|\,.$$

One can further write that:

$$W(t) \leq \omega(t) = \frac{1}{\tau}\int_0^t e^{-\frac{\lambda}{\tau}(t-\nu)}U(\nu)d\nu + e^{-\frac{\lambda}{\tau}t}|x_0|\,,$$

$\forall t \in [0, t_1]$. Finally, considering the upper bound given in (A.9), one has that the following upper bound holds $\forall t \in [0, t_M)$:

$$|x| = W(t) \leq \omega(t) = \frac{1}{\tau}\int_0^t e^{-\frac{\lambda}{\tau}(t-\nu)}U(\nu)d\nu + e^{-\frac{\lambda}{\tau}t}|x_0|\,.$$

■

ISS Property:

Since the ω-dynamics is strictly stable it is clear that is is ISS w.r.t. U. In addition, one has that

$$\omega(t) = \frac{1}{\tau}\int_0^t e^{-\frac{\lambda}{\tau}(t-\nu)}U(\nu)d\nu + e^{-\frac{\lambda}{\tau}t}|x_0|\,,$$

satisfies

$$|\omega(t)| \leq \frac{1}{\lambda}\|U\| + e^{-\frac{\lambda}{\tau}t}|x_0|\,,$$

where the ISS gain $\frac{1}{\lambda} = \lim_{t\to\infty}\frac{1}{\tau}\int_0^t e^{-\frac{\lambda}{\tau}(t-\nu)}d\nu$ is independent of τ.

A.6.2 Ideal Output Variable and ISpS Property: $n^* = 1$

The following lemma can be stated.

Lemma 12 (ISpS property from u_0^{av} to σ) *Consider the σ-dynamics (4.17), with control u_0^{av} given in (4.7) and modulation function in (4.8) satisfying*

$$\varrho \geq |U_d| + \left| \frac{\dot{k}_p}{k_p \kappa_m} \right| |\bar{\sigma}| + \delta \,, \tag{A.10}$$

modulo *vanishing terms, with $\delta > 0$ been an arbitrary constant and $\bar{\sigma}$ in (4.5), then the σ-dynamics (4.17) is ISpS with respect to u_0^{av} and with gain $2\bar{k}_p \tau_{av}$.*

Proof: See Appendix A. From (4.5), one has that $[u_0 - u_0^{av}] = [\dot{\bar{\sigma}} + a_m \bar{\sigma}]/\kappa_m$ and, consequently, one can further write

$$\dot{\epsilon} + a_m \epsilon = k_p[-u_0 + U_d] - \frac{(\kappa_m - k_p)}{\kappa_m}[\dot{\bar{\sigma}} + a_m \bar{\sigma}] \,. \tag{A.11}$$

Now, considering the auxiliary variable $\sigma_b := \epsilon + \frac{(\kappa_m - k_p)}{\kappa_m}\bar{\sigma}$ one has

$$\dot{\sigma}_b + a_m \sigma_b = k_p[-u_0 + U_d] - \frac{\dot{k}_p}{\kappa_m}\bar{\sigma} \,. \tag{A.12}$$

Hence, the time derivative of $V := \sigma_b^2/2$ along the solutions of (A.2) is given by:

$$\dot{V} + 2a_m V = -k_p \sigma_b u_0 + k_p \sigma_b U_d - \sigma_b \left[\frac{\dot{k}_p}{\kappa_m} \right] \bar{\sigma} \,.$$

For $|\epsilon| > \left| \frac{(\kappa_m - k_p)}{\kappa_m} \right| |\bar{\sigma}|$ is is clear that $\text{sgn}(\epsilon) = \text{sgn}(\sigma_b)$ so that $u_0 = \varrho(t)\text{sgn}(\epsilon) = \varrho(t)\text{sgn}(\sigma_b)$. Therefore, $\dot{V}$ satisfies

$$\dot{V} + 2a_m V = -k_p \varrho |\sigma_b| + k_p \sigma_b U_d - \sigma_b \left[\frac{\dot{k}_p}{\kappa_m} \right] \bar{\sigma} \,.$$

and

$$\dot{V} \leq -2a_m V + k_p |\sigma_b| \left\{ -\varrho + |U_d| + \left| \frac{\dot{k}_p}{k_p \kappa_m} \right| |\bar{\sigma}| \right\} \,.$$

If the modulation function ϱ is designed so that

$$\varrho \geq |U_d| + \left| \frac{\dot{k}_p}{k_p \kappa_m} \right| |\bar{\sigma}| + \delta \,,$$

where $\delta > 0$ is a arbitrary positive constant, it is assured that $\dot{V} < -2a_m V$.

Thus, one can conclude via the Comparison Lemma that $|\sigma_b| \leq \pi_{\sigma_b} := |\sigma_b(0)|e^{-a_m t}$.

Now, by noting that $\sigma_b := \epsilon + \frac{(\kappa_m - k_p)}{\kappa_m}\bar{\sigma} = \sigma - \bar{\sigma} + \frac{(\kappa_m - k_p)}{\kappa_m}\bar{\sigma} = \sigma - \frac{k_p}{\kappa_m}\bar{\sigma}$ one can subsequentelly write

$$|\sigma - \frac{k_p}{\kappa_m}\bar{\sigma}| \leq |\sigma(0) - \frac{k_p(0)}{\kappa_m}\bar{\sigma}(0)|e^{-a_m t}\,,$$

and

$$|\sigma| - |\frac{k_p}{\kappa_m}\bar{\sigma}| \leq \pi_\sigma + \frac{\bar{k}_p}{\kappa_m}\pi_{\bar{\sigma}}\,,$$

and

$$|\sigma| \leq \frac{\bar{k}_p}{\kappa_m}|\bar{\sigma}| + \pi_\sigma + \frac{\bar{k}_p}{\kappa_m}\pi_{\bar{\sigma}}\,,$$

where $\pi_\sigma := |\sigma(0)|e^{-a_m t}$ and the upper bound given in (4.15) were used.

From Lemma 1, one has that $\bar{\sigma}$-dynamics is ISS w.r.t. u_0^{av}. So, the σ-dynamics ISpS w.r.t. u_{av} with gain $2\bar{k}_p\tau_{av}$, provided that $|\epsilon| > \left|\frac{(\kappa_m - k_p)}{\kappa_m}\right| |\bar{\sigma}|$.

For the case $|\epsilon| \leq \left|\frac{(\kappa_m - k_p)}{\kappa_m}\right| |\bar{\sigma}|$, one has that

$$|\sigma| - |\bar{\sigma}| \leq |\sigma - \bar{\sigma}| = |\epsilon| \leq \left|\frac{(\kappa_m - k_p)}{\kappa_m}\right| |\bar{\sigma}|\,,$$

and, thus, one can obtain the norm bound

$$|\sigma| \leq |\bar{\sigma}| + \left|\frac{(\kappa_m - k_p)}{\kappa_m}\right| |\bar{\sigma}|\,,$$

which leads to the conclusion that the σ-dynamics ISpS w.r.t. u_{av} with gain proportional to τ_{av}, by considering Lemma 1. ∎